Marine Boundary Layers above Heterogeneous SST: Across-Front Winds

PETER P. SULLIVAN,[a] JAMES C. MCWILLIAMS,[b] JEFFREY C. WEIL,[a] EDWARD G. PATTON,[a] AND HARINDRA J. S. FERNANDO[c]

[a] *National Center for Atmospheric Research, Boulder, Colorado*
[b] *Department of Atmospheric and Oceanic Sciences, University of California, Los Angeles, Los Angeles, California*
[c] *Department of Civil and Environmental Engineering and Earth Sciences, University of Notre Dame, South Bend, Indiana*

(Manuscript received 28 February 2020, in final form 14 July 2020)

ABSTRACT: Turbulent flow in a weakly convective marine atmospheric boundary layer (MABL) driven by geostrophic winds $U_g = 10\,\mathrm{m\,s^{-1}}$ and heterogeneous sea surface temperature (SST) is examined using fine-mesh large-eddy simulation (LES). The imposed SST heterogeneity is a single-sided warm or cold front with temperature jumps $\Delta\theta = (2, -1.5)$ K varying over a horizontal distance between $[0.1, -6]$ km characteristic of an upper-ocean mesoscale or submesoscale regime. A Fourier-fringe technique is implemented in the LES to overcome the assumptions of horizontally homogeneous periodic flow. Grid meshes of 2.2×10^9 points with fine-resolution (horizontal, vertical) spacing $(\delta x = \delta y, \delta z) = (4.4, 2)$ m are used. Geostrophic winds blowing across SST isotherms generate secondary circulations that vary with the sign of the front. Warm fronts feature overshoots in the temperature field, nonlinear temperature and momentum fluxes, a local maximum in the vertical velocity variance, and an extended spatial evolution of the boundary layer with increasing distance from the SST front. Cold fronts collapse the incoming turbulence but leave behind residual motions above the boundary layer. In the case of a warm front, the internal boundary layer grows with downstream distance conveying the surface changes aloft and downwind. SST fronts modify entrainment fluxes and generate persistent horizontal advection at large distances from the front.

KEYWORDS: Atmosphere-ocean interaction; Boundary layer; Fronts; Marine boundary layer; Sea surface temperature; Surface layer

1. Introduction

Imagery, observations, and simulations find an active spatially heterogeneous ocean surface populated by a ubiquitous collection of coherent flow structures of varying scale (Chelton et al. 2004; Gula et al. 2014; McWilliams 2016; Bishop et al. 2017). A striking example is submesoscale ocean turbulence, a relatively recent discovery, that features persistent fronts, filaments, and vortices with scales in the range [0.1–10] km (see review by McWilliams 2016). These submesoscale structures as well as larger-scale ocean eddies generate long-lived sharp horizontal gradients in the ocean surface buoyancy and current fields. And these gradients are found to impact the curl and divergence of wind stress (Chelton et al. 2004; O'Neill et al. 2010), the correlation between wind speed and sea surface temperature (SST) fluctuations (Chelton and Wentz 2005; Gemmrich and Monahan 2018; Gaube et al. 2019; Shao et al. 2019; Redelsperger et al. 2019; Meroni et al. 2020), boundary layer convergence at large scales (Kilpatrick et al. 2014), and atmosphere–ocean coupling (Spall 2007; Plagge et al. 2016; Seo et al. 2016; Renault et al. 2019; Skyllingstad et al. 2019). The positive correlation between wind speed and SST often found by investigators suggests that the usual atmosphere–ocean coupling is reversed; that is, a heterogeneous ocean is capable of driving the atmosphere at smaller scales. Coupled air–sea mesoscale models developed by Seo et al. (2016) and Renault et al. (2019) include both current and thermal couplings. They find current coupling produces a surprisingly strong feedback on the ocean, weakening the strength of ocean eddies. From an oceanic perspective understanding the influence of SST gradients on near surface winds is important (Gill 1982; Chelton et al. 2004). SST gradients change the atmospheric stability, hence the wind profile and surface stress, and these changes can drive anomalous responses in oceanic boundary layer currents.

Air–sea coupling, accounting for a wavy interface (Sullivan and McWilliams 2010) and ocean heterogeneity, is a broadband space–time process fundamentally rooted in the turbulent marine atmospheric boundary layer (MABL) and oceanic boundary layer (OBL) and remains an important research area for improving weather forecasts and climate predictions (Small et al. 2008). Ocean submesoscale heterogeneity is subgrid in global models, and by necessity these models rely on single column mixing schemes as part of their boundary layer parameterizations. The fidelity of the boundary layer schemes is unknown with surface heterogeneity. Perlin et al. (2014) concludes that the MABL parameterization must be given careful consideration when modeling the atmospheric response to SST gradients.

Past work provides clues about the impact of heterogeneous SST on the MABL. Aircraft observations by Khalsa and Greenhut (1989) and Friehe et al. (1991) find a dependence on the wind–SST orientation; that is, different boundary layer motions including secondary circulations are found when winds blow perpendicular or parallel to the SST isotherms. Also, the investigators find a reduction in wave height in a warm–cold transition due to diminished surface fluxes and wind speed. However, the limited sampling available from aircraft observations hinders the ability to create stationary statistics from these highly turbulent fields. There is a large

Corresponding author: Peter P. Sullivan, pps@ucar.edu

DOI: 10.1175/JAS-D-20-0062.1

body of prior work examining the impact of heterogeneous step changes in land surfaces on the atmospheric boundary layer (see Garratt 1994; Kaimal and Finnigan 1994). A notable example is the heterogeneous wind-driven stable Arctic boundary layer, which is strongly variable depending on the vigorous convective plumes that develop over open water finite-width leads. Lüpkes et al. (2008) and Tetzlaff et al. (2015) report nonlinear variation of vertical fluxes, enhanced entrainment, and complex spatial boundary layer evolution depending on the lead scale and downwind fetch.

The present work focuses on the response of unstable and stably stratified turbulent MABLs forced by heterogeneous SST at small horizontal scales. Process studies are carried out using fine-mesh large-eddy simulation (LES) in large horizontal domains, which allows us to examine turbulent momentum and scalar transport in the MABL close to and distant from the location of the SST heterogeneity. Mean horizontal and vertical advection are important above heterogeneous surfaces and LES permits examination of boundary layer dynamics in regimes where assumptions in single-column mixing schemes are often violated (e.g., Lüpkes et al. 2008). Horizontal periodicity is the usual assumption in the majority of LES; it is easy to implement, requires no special treatment in the governing equations, and by construction generates turbulent inflow and outflow conditions. However, horizontal periodicity has the drawback that spatially growing or decaying boundary layers cannot be cleanly captured, for example, there are no mean horizontal gradients in a typical periodic code. To circumvent periodicity constraints, approximate "Lagrangian" approaches are often adopted that advect a full periodic LES domain by a time varying large-scale wind (e.g., Lin et al. 1997; Skyllingstad et al. 2005; Small et al. 2008; Jiang et al. 2020). Skyllingstad et al. (2007) used open boundary conditions and the single plane perturbation recycling method described by Mayor et al. (2002) to examine the response of boundary layer winds crossing a stepwise pattern of SST jumps each of width 10 km; because of computational cost, their LES domain was restricted in the spanwise and vertical dimensions. Wenegrat and Arthur (2018) used the LES option in the Weather Research and Forecasting (WRF) code to study the MABL response with down-front winds; their horizontal mesh is relatively coarse $\delta \sim 20$ m and the horizontal domain was doubly periodic. In the present work, the horizontal scale in the LES extends to 30 km or more with horizontal spacing $\delta \sim 4.4$ m. And we use a variant of the numerical "Fourier-fringe" technique that permits simulations of spatially evolving, nonperiodic, turbulent boundary layers with varying turbulent inflow conditions (see discussion and references in section 3). Boundary layer regimes with geostrophic winds flowing across the SST isotherms, referred to as across-front winds, are considered.

The outline of the paper is as follows: the LES equations appropriate for a high-Reynolds-number MABL are introduced in section 2, a brief introduction to the Fourier-fringe technique is given in section 3, and the suite of LES experiments is described in section 4. Evaluation of the Fourier-fringe method is provided in section 5, results are discussed in section 6, and section 7 provides a summary and conclusions.

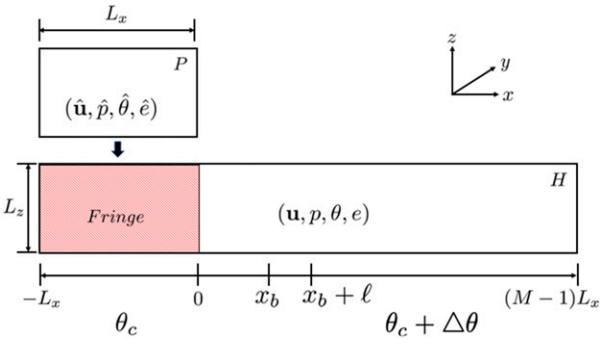

FIG. 1. Sketch of periodic P and heterogeneous H LES domains used to simulate a spatially developing nonperiodic marine atmospheric boundary layer; adapted from Inoue et al. (2014). The sizes of the domains are (L_x, L_y, L_z) and (ML_x, L_y, L_z) with $M = 7$, 10. The field variables in P are denoted $(\hat{\mathbf{u}}, \hat{p}, \hat{\theta}, \hat{e})$ and in H are denoted $(\mathbf{u}, p, \theta, e)$. In the fringe region of H, solution variables in P and H are linearly blended using the rule (2), which assigns greater weight to the fields in P. In P the imposed surface temperature is θ_c. In H the surface temperature is heterogeneous, θ_c is linearly incremented by $\Delta\theta$ over a distance ℓ starting at the break point $x = x_b$ located east of the fringe region; see (5).

2. LES governing equations

The LES model for the MABL adapted to account for a heterogeneous ocean surface is derived from our suite of codes used to simulate atmospheric and oceanic boundary layers, recent descriptions are given by Sullivan and Patton (2011); Sullivan et al. (2014, 2016); Sullivan and McWilliams (2019). A brief description of the LES equations and solution algorithm is given to introduce the coordinate system and variables used in the simulations and analysis, see Fig. 1; further simulation details are in section 4.

The following notation is used: $\mathbf{u} \equiv u_i = (u, v, w)$ denote the Cartesian velocity components, θ is virtual potential temperature, and p is the pressure variable normalized by density ρ. The three Cartesian coordinates are $\mathbf{x} \equiv x_i = (x, y, z)$ and are referred to as (streamwise, spanwise, vertical) directions, respectively. The set of LES equations that describe rotating stratified turbulent flow in a MABL under the incompressible Boussinesq approximation are

$$\frac{\partial \mathbf{u}}{\partial t} = -\mathbf{u}\cdot\nabla\mathbf{u} - \mathbf{f}\times(\mathbf{u}-\mathbf{U}_g) - \nabla p + \mathbf{z}\beta(\theta-\theta_o) - \nabla\cdot\mathbf{T}, \tag{1a}$$

$$\frac{\partial \theta}{\partial t} = -\mathbf{u}\cdot\nabla\theta - \nabla\cdot\mathbf{B}, \tag{1b}$$

$$\frac{\partial e}{\partial t} = -\mathbf{u}\cdot\nabla e + \mathscr{P} + \mathscr{B} + \mathscr{D} - \mathscr{E}, \tag{1c}$$

$$\nabla\cdot\mathbf{u} = 0. \tag{1d}$$

The above equation set includes transport equations for momentum $\rho\mathbf{u}$, (1a); virtual potential temperature θ, (1b); and subgrid-scale (SGS) turbulent kinetic energy e, (1c). The divergence free (incompressible) condition, (1d), determines the elliptic pressure variable p. Equation (1) also includes geostrophic

winds $\mathbf{U}_g = (U_g, V_g)$, rotation vector $\mathbf{f} = (0, 0, f)$ with Coriolis parameter f, unit vector $\mathbf{z}$ in the vertical direction, and buoyancy parameter $\beta = g/\theta_o$, where g is gravity and θ_o is the reference potential temperature. The transport equation, (1c), for SGS e contains a standard set of right-hand-side terms: production $\mathscr{P}$, buoyancy $\mathscr{B}$, diffusion $\mathscr{D}$, and viscous dissipation $\mathscr{E}$. The modeling of these terms is not repeated here and can be found in Sullivan et al. (1994); McWilliams et al. (1999); Moeng and Sullivan (2015). SGS momentum and temperature fluxes ($\mathbf{T}$, $\mathbf{B}$) are estimated using turbulent eddy viscosity prescriptions $(\nu_t, \nu_\theta) \sim \ell\sqrt{e}$, where ℓ is a stability corrected length scale. The LES equations are formally derived by applying a spatial filter to the Navier–Stokes equations. To streamline the notation, the standard overbar notation $\overline{(\cdots)}$ indicating spatial filtering in (1), is dropped and we refer to virtual potential temperature θ simply as "temperature."

Near the top of the LES domain, we impose a sponge layer to suppress reflections from the upper boundary (e.g., Durran 1999). A damping term of the form $\sigma_d(z)(\langle\Psi\rangle - \Psi)$ is added to the right-hand side of each transport equation where $\langle\Psi\rangle$ denotes an average over a horizontal x–y plane: $\Psi = (\mathbf{u}, \theta, e)$ as appropriate. The inverse time scale σ_d decays to zero quadratically from its maximum value at the upper boundary over a distance of 20% of the vertical domain. As is common practice, at the lower boundary we impose rough wall boundary conditions based on bulk aerodynamic formulas where the transfer coefficients are determined from Monin–Obukhov (M-O) similarity functions (Moeng 1984). The M-O rules are applied point-by-point at the lower boundary as described by Sullivan et al. (2014) and Mironov and Sullivan (2016) with imposed SST as the boundary condition. In the x direction, turbulent inflow–outflow boundary conditions are prescribed by the fringe implementation described in section 3.

We utilize well established algorithms to integrate the LES Eqs. (1); see McWilliams et al. (1999), Sullivan and Patton (2011), Moeng and Sullivan (2015), and the references cited therein. The equations are advanced in time using an explicit fractional step method that enforces incompressibility at every stage of the third-order Runge–Kutta (RK3) scheme. Dynamic time stepping with a fixed Courant–Fredrichs–Lewy (CFL) is used (Sullivan et al. 1996). The spatial discretization is second-order finite difference in the vertical direction and pseudospectral in horizontal planes.

3. Fourier-fringe method

The Fourier-fringe method is a general recipe for simulating spatially evolving (nonperiodic) turbulent boundary layers in finite domains using traditional Fourier methods. Essentially, the method is an artificial boundary condition in the same spirit as filters, sponge layers, or windowing, see Nordström et al. (1999); Schlatter et al. (2005). The method is flexible, it can be used to impose laminar or turbulent inflow–outflow conditions on the computational domain of interest. Implementations attach a separate finite length fringe region to the primary computational domain, and in the fringe region, forcing functions are applied to nudge the velocity and scalar fields toward prescribed inflow–outflow conditions. A positive feature is that Fourier (periodic) methods are retained with no special treatment of the governing equations, thus traditional pseudospectral boundary layer codes can be used (e.g., Sullivan and Patton 2011). Spalart and Watmuff (1993) first proposed the fringe approach and successfully used the technique to perform direct numerical simulation (DNS) of a spatially growing smooth-wall boundary layer. Nordström et al. (1999) analyzed the mathematical properties of the Fourier-fringe method and find that it leads to well-posed computational problems. In geophysical applications, Inoue et al. (2014) generate fully turbulent inflow conditions using rough-wall LES and use the fringe approach to study the spatial transition of a cloud-topped boundary layer. Munters et al. (2016) also propose a fringe scheme that uses LES and a separate doubly periodic so-called precursor simulation to generate turbulent inflow conditions for spatially heterogeneous wind park applications; the authors also nicely compare the spatial variability of inflow fields generated by synthetic methods versus those generated by Navier–Stokes solvers (see Fig. 1 of Munters et al. 2016). Inflow turbulence produced by LES or DNS contains large-scale coherent structures that vary with stratification and thus is a preferred method for generating a three-dimensional time-dependent turbulent inflow, but is clearly a computationally more expensive approach to turbulence generation compared to synthetic methods (e.g., Muñoz-Esparza et al. 2015).

a. Fringe algorithm

Our implementation of the Fourier-fringe method follows the developments outlined in the previous section but is tailored toward our investigation focusing on the impact of heterogeneous sea surface conditions on the MABL. We utilize two LES domains (P, H) as sketched in Fig. 1, the overlapping fringe region between the two domains is shown in red. LES variables in the P domain are indicated by $\widehat{(\cdots)}$. The computational domains are 3D but for clarity only x–z cross sections are shown in Fig. 1. The domains (P, H) are each doubly periodic but differ in size; P has horizontal extent $L_x = L_y$, while domain H has dimensions $(M \times L_x, L_y)$, where $M > 1$ is a large multiplier, typically $M = 7$ or 10. Each domain spans the same vertical extent L_z. The surface heterogeneity is imposed at the lower boundary in H as shown in Fig. 1; notice the streamwise coordinate $x = [-1, (M - 1)]L_x$. The LES in domain P generates time-varying fully developed stratified turbulence typical of an atmospheric boundary layer and provides inflow conditions for H. The communication between P and H is one way: P drives H. In our parallel code, separate Message Passing Interface (MPI) communicators (Gropp et al. 1998) run LES in domains (P, H) concurrently using the same shared time step and spatial discretization.

b. Fringe forces

In the fringe region of H, forces are added to the velocity and scalar transport equations:

$$\frac{\partial \mathbf{u}}{\partial t} = \mathscr{R}(\mathbf{u}, \theta) - \nabla p + \lambda(x)(\hat{\mathbf{u}} - \mathbf{u}), \tag{2a}$$

$$\frac{\partial \theta}{\partial t} = \mathscr{S}(\mathbf{u}, \theta) + \lambda(x)(\hat{\theta} - \theta), \tag{2b}$$

$$\frac{\partial e}{\partial t} = \mathscr{T}(\mathbf{u}, \theta) + \lambda(x)(\hat{e} - e). \tag{2c}$$

In (2), $(\mathscr{R}, \mathscr{S}, \mathscr{T})$ denote the complete right side of the LES Eqs. (1), minus the pressure gradients in (1a); the fringe forces depend on the pointwise difference between fields in P and H. After the right-hand side of (2a) is evaluated, the pressure update is completed by applying the usual recipe for our explicit fractional step method (Sullivan et al. 1996; Sullivan and Patton 2011). Separate pressure Poisson equations in the (P, H) domains, derived by applying the discrete divergence operator (1d) to (2a), are solved using Fourier decomposition in horizontal planes followed by a tridiagonal matrix inversion in the vertical direction. At the new time step $\nabla \cdot (\mathbf{u}, \hat{\mathbf{u}}) \equiv 0$.

The shape and amplitude of the added forces are designed so that the fields in H are smoothly nudged toward the fields in P. As suggested by Nordström et al. (1999) we use the smooth blending function

$$\lambda(x) = A\left[Q\left(\frac{x+L_x}{L_x d_{\text{rise}}}\right) - Q\left(\frac{x}{L_x d_{\text{fall}}}+1\right)\right], \tag{3}$$

where

$$Q(\xi) = \begin{cases} 0, & \xi < 0, \\ \dfrac{1}{\left[1+\exp\left(\dfrac{1}{\xi-1}+\dfrac{1}{\xi}\right)\right]}, & 0 < \xi < 1, \\ 1, & \xi \geq 1. \end{cases} \tag{4}$$

Outside the fringe region $\lambda(x) = 0$. Parameters $(d_{\text{rise}}, d_{\text{fall}})$ determine the rise and fall rates of the blending and the amplitude parameter A (units of s^{-1}) is an inverse time scale that controls the strength of the nudging, that is, how strongly the fields in H are pushed toward the fields in P. Different rise and fall rates produced only small changes and for the majority of the simulations we set $(d_{\text{rise}}, d_{\text{fall}}) = (0.5, 0.5)$. The amplitude A is the key nudging parameter. For the imposed winds and spatial discretization the nominal time step of the calculations $\Delta t \sim 0.20\,\text{s}$, and we set $A = 1\,\text{s}^{-1}$. Results in section 5 show $A = 1\,\text{s}^{-1}$ is strong nudging but the magnitude of A is well below the maximum value estimated by Schlatter et al. [2005, Eq. (8)] for third-order Runge–Kutta schemes, $A\Delta t < 2.51$. The SST heterogeneity is assumed to be homogeneous in y, and as a result the blending function varies only with Δx A discussion of the adequacy of the Fourier-fringe method in the present application is postponed to section 5.

4. LES process studies

The design of the LES experiments largely follows our prior work (e.g. Sullivan and Patton 2011; Sullivan et al. 2016). Here we examine the impact of heterogeneous SST, that is, SST fronts, on the MABL. The SST fronts are time invariant, vary solely in the x direction, and single-sided fronts with jumps between two temperature levels over a finite x distance are imposed. For discussion, a set of horizontal directions are defined relative to the axis of the SST isotherms. The directions (perpendicular, parallel) to the isotherms are referred to as (across, down) the SST front, respectively. In the LES, the imposed geostrophic wind is across-front $U_g = 10\,\text{m s}^{-1}$, the Coriolis parameter $f = 10^{-4}\,\text{s}^{-1}$, and the roughness $z_o = 2\times10^{-4}\,\text{m}$ is picked to be representative of a wavy ocean surface based on winds $\leq 10\,\text{m s}^{-1}$ (Large and Pond 1981). There is no large-scale imposed subsidence.

TABLE 1. Simulation properties in P domain.

Case	(U_g, V_g) (m s^{-1})	$\widehat{u_*}$ (m s^{-1})	$\widehat{Q_*}$ (K m s^{-1})	$\widehat{w_*}$ (m s^{-1})	$\hat{z}_i$ (m)	$-\hat{L}$ (m)	$-\hat{z}_i/\hat{L}$
E	(10, 0)	0.286	0.0115	0.602	560.3	150.0	3.74

Heterogeneous $\theta_s(x, y)$ with multiple jumps, surface currents, surface waves, and surface roughness z_o changes are some of the many important variants not considered here but can be included in straightforward fashion in the present computational framework.

In H (see Fig. 1), the distribution of sea surface temperature θ_s for a single front is given by the rule

$$\theta_s(x) = \begin{cases} \theta_c & : -L_x < x < x_b \\ \theta_c + \dfrac{\Delta\theta}{\ell}(x - x_b) & : x_b < x < x_b + \ell, \\ \theta_c + \Delta\theta & : x \geq x_b + \ell \end{cases} \tag{5}$$

where the constant $\theta_c = 290.17\,\text{K}$, $\Delta\theta$ is the magnitude of the SST jump over the length scale ℓ, and $x_b = 0.8L_x = 2700\,\text{m}$ marks the start of the jump. Because of mesoscale and submesoscale turbulence the spatial distribution of SST is highly variable, and it is infeasible to investigate all the many variants in our computations. Thus, we simply choose typical examples of positive and negative SST jumps. Gradients in SST are created by fixing $\Delta\theta = (2, -1.5)\,\text{K}$ and varying $\ell = [0.1\text{–}6]\,\text{km}$ [the specific combinations of $(\Delta\theta, \ell)$ are listed in Table 2].

Domain P is $(L_x, L_y, L_z) = (3.375, 3.375, 1.4)\,\text{km}$ and is discretized with a grid mesh $(N_x, N_y, N_z) = (768, 768, 384)$ grid points. Domain H is $(10L_x, L_y, L_z) = (33.75, 3.375, 1.4)\,\text{km}$ and is discretized with a grid mesh $(10N_x, N_y, N_z) = (7680, 768, 384)$ grid points; we also use a smaller H domain with horizontal extent $7L_x$ and $7N_x = 5376$ grid points. In both P and H the horizontal spacing is constant $\Delta x = \Delta y = 4.4\,\text{m}$, while the spacing between grid points Δz in the vertical mesh varies smoothly using the constant stretching factor $K = \Delta z_{i+1}/\Delta z_i = 1.002\,88$; the first w-grid level $z_1 = 2\,\text{m}$.

Statistics are computed in both (P, H) domains. In P statistics are obtained by spatial averaging over its full horizontal x–y domain, and by averaging in time. We use the notation $\widehat{\langle\cdots\rangle}$ to indicate this averaging. For clarity, average surface-layer variables and boundary layer height in P omit the $\langle\cdots\rangle_{xy}$ notation. Table 1 is a compilation of computed bulk statistics from P, namely, friction velocity $\widehat{u_*}$, temperature flux $\widehat{Q_*}$, convective velocity scale $\widehat{w_*}$, boundary layer depth $\hat{z}_i$, and stability parameter $\hat{z}_i/\hat{L}$, where the Monin–Obukhov length $\hat{L} = -\widehat{u_*}^3/\beta\kappa\widehat{Q_*}$, with β as the buoyancy parameter and von Kármán constant $\kappa = 0.4$. The convective velocity scale $\widehat{w_*}^3 = \beta\widehat{Q_*}\hat{z}_i$ (Deardorff 1970), and the boundary layer height $\hat{z}_i$ is estimated based on the vertical location of the maximum temperature gradient (Sullivan et al. 1998). The statistics in the P domain are used for normalization. Based on the values in

TABLE 2. SST variations in heterogeneous H domain.

Case	ℓ (m)	$\Delta\theta$ (K)	$(x_b, x_b + \ell)$ (m)	$\hat{z}_i/\ell$
Eu1	100	2	(2700, 2800)	5.6
Eu2	1000	2	(2700, 3700)	0.56
Eu3	3000	2	(2700, 5700)	0.19
Eu4	6000	2	(2700, 8700)	0.09
Es1	100	−1.5	(2700, 2800)	5.6
Es2	1000	−1.5	(2700, 3700)	0.56

Tables 1 and 2 the ratio of boundary layer height to frontal width in our experiments varies by more than a factor of 50, $\hat{z}_i/\ell = [5.6\text{–}0.09]$.

In the H domain, the spatial inhomogeneity in the x direction complicates the analysis of the LES solutions. To diagnose mean and turbulence fields in statistics and flow visualization we use a combination of time and restricted space averaging (e.g., see Sullivan and McWilliams 2019). At any time step, we first project the flow fields onto an x–z plane by spatial averaging in the homogeneous y direction; this averaging is indicated by angle brackets $\langle \cdots \rangle$. Any variable f is then decomposed into a mean $\langle f \rangle$ and fluctuation f' by

$$f(\mathbf{x}) = \langle f \rangle(x, z) + f'(\mathbf{x}). \tag{6}$$

Products of flow variables, as well as momentum and temperature budgets, are also constructed using (6). Both mean values and correlations contribute to vertical fluxes and variances, for example,

$$\langle fw \rangle - \langle f \rangle \langle w \rangle = \langle f'w' \rangle, \quad \text{and} \quad \langle ff \rangle - \langle f \rangle \langle f \rangle = \langle f'f' \rangle. \tag{7}$$

The LES code is configured to compute means, variances, fluxes, and other statistics during the run based on (6) and (7). The resulting x–z planes of data are archived at much finer time resolution compared to the full 3D volumes. To improve convergence of the statistics, the x–z planes of data are further averaged in time using postprocessing codes.

A special recipe is used to build the initial conditions for the simulations in H. First, the LES in domain P is run independently

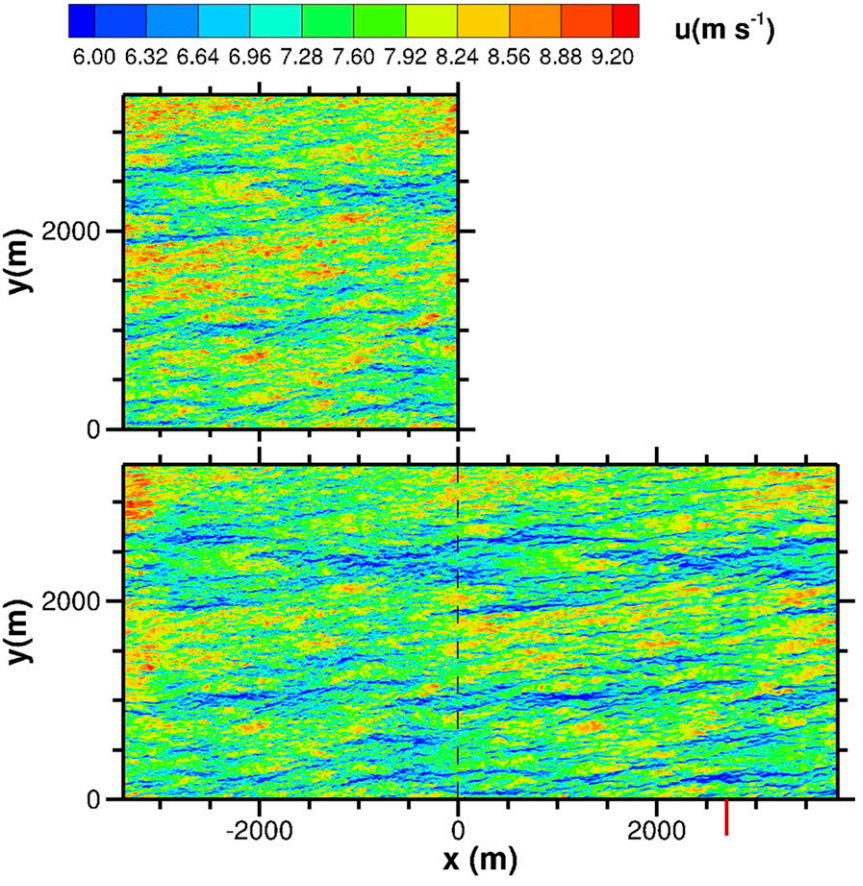

FIG. 2. Visualization of the instantaneous streamwise velocity u in an x–y plane for simulation Eu1: (top) domain P and (bottom) domain H showing a small fraction of the horizontal extent. In the bottom panel, the black dotted vertical line shows the right boundary of the fringe region and the red vertical bar at the bottom marks the location $x = x_b$ where the surface temperature starts to increase. The time is $t \sim 9320$ s, the vertical location is $z = 12$ m, and the dominant direction of the surface wind is left to right.

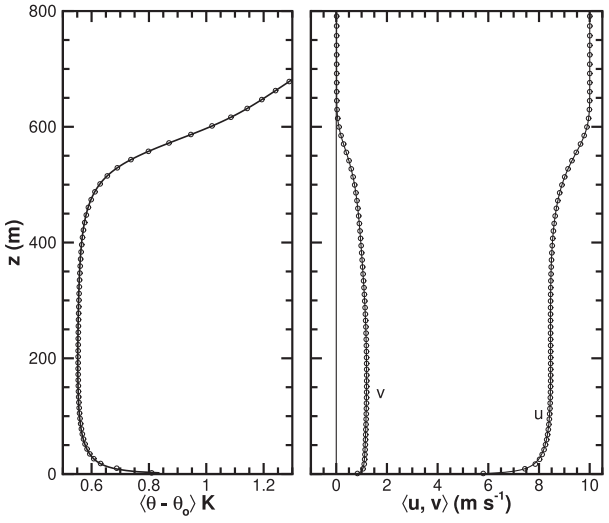

FIG. 3. Comparison of the mean (left) temperature and (right) wind profiles from the periodic and heterogeneous domains. The time–spatial averaging in the periodic domain is over the full x–y domain and in the heterogeneous domain over y and $x = [675, 2700]$ m. The results from the P and H domains are shown with solid lines and open circles, respectively. The boundary layer height $\widehat{z}_i = 560$ m.

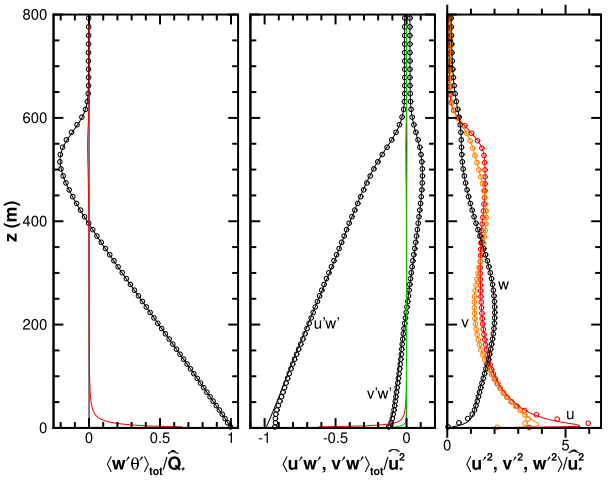

FIG. 4. Comparison of turbulence statistics in the (P, H) domains over the the same horizontal domains as in Fig. 3. (left) Total (resolved plus SGS) temperature flux $\langle w'\theta'\rangle_{\rm tot}$ normalized by the surface flux $\widehat{Q}_*$ in the periodic domain, (center) total momentum fluxes $\langle u'w', v'w'\rangle_{\rm tot}$ normalized by $\widehat{u}_*^2$ in the periodic domain, and (right) the resolved variances $\langle u'^2, v'^2, w'^2\rangle$ normalized by $\widehat{u}_*^2$ in the periodic domain. Profiles from the P and H domains are indicated by solid lines and open circles, respectively. The SGS temperature flux $\langle\tau_{w\theta}\rangle/\widehat{Q}_*$ is denoted by the red line in the left panel, and the SGS momentum fluxes $\langle\tau_{uw}\rangle/\widehat{u}_*^2$ and $\langle\tau_{vw}\rangle/\widehat{u}_*^2$ are denoted by solid red and solid green lines, respectively, in the center panel. The SGS fluxes are from the P domain.

with an unstable surface temperature flux $Q_* = 0.015\,\mathrm{K\,m\,s^{-1}}$ and $U_g = 10\,\mathrm{m\,s^{-1}}$. The initial stratification profile is two linear segments, $\theta = \theta_c$ for $0 < z < \widetilde{z}_i$ and $\theta = \theta_c + (z - \widetilde{z}_i)\partial_z\theta$ for $z > \widetilde{z}_i$ with $\theta_c = 290$ K, $\widetilde{z}_i = 250$ m, and $\partial_z\theta = 0.003\,\mathrm{K\,m^{-1}}$. This initial profile (e.g., Schmidt and Schumann 1989) facilitates realistic boundary layer growth with a boundary layer depth ~ 500 m as the turbulence nears a quasi-equilibrium state. The integration time for the spinup is approximately 6500 s, which is sufficient to generate fully developed turbulence typical of a weakly unstable MABL (e.g., Sullivan et al. 2014). The last data volume from the spinup simulation is archived and used as the initial condition for simulations in P and H; the volume is replicated M times for the initial condition in H. This initialization recipe is inexpensive and provides a high quality estimate of the flow state in the H domain. Finally, the LES is restarted but now with θ_s given by (5) as the surface boundary condition. The restart produces an onset transient that rapidly leaves the domain. The simulations in P and H run concurrently with one-way coupling from P to H in the fringe region, and the simulations are run for approximately 18 000 s. Based on ($\widehat{w}_*$, $\widehat{z}_i$) in Table 2 this integration time is ~12 large-eddy turnover times. Inspection of the time series of bulk variables and vertical profiles shows that the flow in the H domain is near quasi-equilibrium after 3600 s. The statistics presented here are collected over the last 5400 s of the simulation, ~6 large-eddy turnover times, see Table 2.

5. Outflow turbulence downstream of the fringe

The Fourier-fringe method controls the (inflow, outflow) turbulence at the far (left, right) boundaries of domain H. At every time step inside the fringe region $-L_x < x < 0$, the turbulent fields flowing into H from the left boundary are first damped and then smoothly nudged toward the target turbulent fields in P with the transition dependent on $\lambda(x)$. For our choice of fringe parameters, how well does the scheme work and what kind of turbulence does it generate in H? Recall the surface boundary conditions, roughness, as well as the geostrophic winds imposed in H and P are matched in the interval $-L_x < x < x_b$, see Fig. 1. Then to test the adequacy of the fringe method in setting the desired inflow conditions we can compare the fields in H, just outside of the fringe over the interval $0 < x < x_b$, with their counterparts in P. A typical instantaneous picture of the u flow field from P and H is presented in Fig. 2. This image is an x–y slice taken from simulation Eu1 at $z = 12$ m. The aspect ratio of the images is unity, only a small fraction of the entire H domain is shown, and the time is late in the simulation. In the bottom panels, the (black dotted, solid white) lines at $x = (0, 2700)$ m mark the end of the fringe and the start location x_b of the SST jump, respectively.

The flow fields in P are typical of fully developed stratified wall turbulence generated by LES. At a bulk stability $-\widehat{z}_i/\widehat{L} = 3.7$, the combination of shear and convective forcing produces organized coherent streaky flow patterns superimposed on a background of smaller-scale random turbulent motions, (e.g., see Moeng and Sullivan 1994; Fedorovich et al. 2001; Sullivan et al. 2014). These organized structures are ubiquitous in weak and moderately forced shear–convective boundary layers and are also readily inferred from observations of organized cloud patterns over the ocean (e.g., Chen

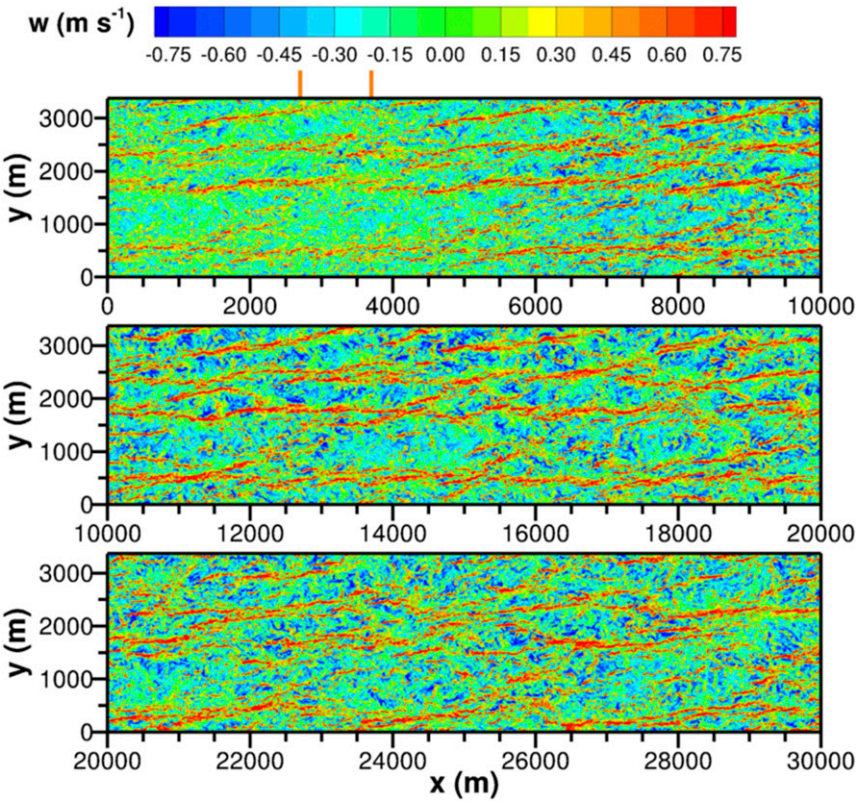

FIG. 5. Vertical velocity w in an x–y plane evolving over a warm SST jump, in simulation Eu2. The full H domain is depicted, but for visualization is split into three panels each spanning 10 km of the domain. The x–y slice is near the surface layer at $z = 50$ m. (top) The orange vertical lines show the start and end of the SST jump $\Delta\theta = 2$ K spanning $\ell = 1000$ m.

et al. 2001). Inspection of Fig. 2 shows that the fringe forces damp the turbulence at the left boundary of H and induce a smooth transition toward the turbulence in P at every interior gridpoint location. Inside the fringe region of H the flow fields are of course spoiled. Downstream of the fringe the structures and flow patterns in H are similar to their counterparts in P. Similar good comparisons are found at other z locations and times, and in other flow variables.

Time and space averaged statistics are used to assess the state of the inflow turbulence in domain H compared to P. A comparison of the vertical profiles of mean winds $\langle u, v\rangle$ and temperature $\langle\theta\rangle$ is shown in Fig. 3. Vertical profiles of temperature and momentum fluxes and $\langle w'\theta', u'w', v'w', u'^2, v'^2, w'^2\rangle$ variances are compared in Fig. 4; note the momentum and temperature fluxes include both resolved and SGS contributions and the normalization in the three panels is by $(\widehat{Q_*}, \widehat{u_*^2})$. At each z level, the statistics are generated by a time average over the last 5400 s of the simulation and a spatial average over a horizontal plane. In H the spatial average is over $(x, y) = [(675–2700), 3375]$ m, where θ_s is constant while the spatial average in P is over its entire horizontal domain $(x, y) = (3375, 3375)$ m. The agreement between the mean fields and also the low-order turbulence moments in P and H is excellent.

Slight variations of a standard one-equation TKE model for SGS fluxes are used in the different LES domains. In P the flow is assumed horizontally homogeneous and M-O similarity theory is applicable. Thus, we use the two-part eddy viscosity model (Sullivan et al. 1994) that includes a wall correction and reproduces M-O mean profiles in the surface layer. In domain H, which is horizontally heterogeneous, the applicability of M-O theory is unknown and thus we use a standard TKE model with no wall corrections (Moeng 1984). The change in SGS models causes small differences in the momentum flux $\langle u'w'\rangle$ very near the surface. The mesh resolution in the LES is fine and SGS fluxes are small in the bulk of the flow as shown in Fig. 4.

Overall the fringe scheme provides excellent control of the inflow and outflow turbulence in H. Downstream of the fringe region the flow fields contain realistic 3D time-varying coherent structures and turbulence; the mean and turbulence statistics in H are also in excellent agreement with those from a similarly forced horizontally homogeneous boundary layer.

6. Results with across-front winds

a. Vertical velocity patterns

Warm and cold SST fronts influence the structure of the instantaneous flowfields, effects that are readily observed in flow visualization and time animations. Owing to space constraints, only a small subset of the visualization data

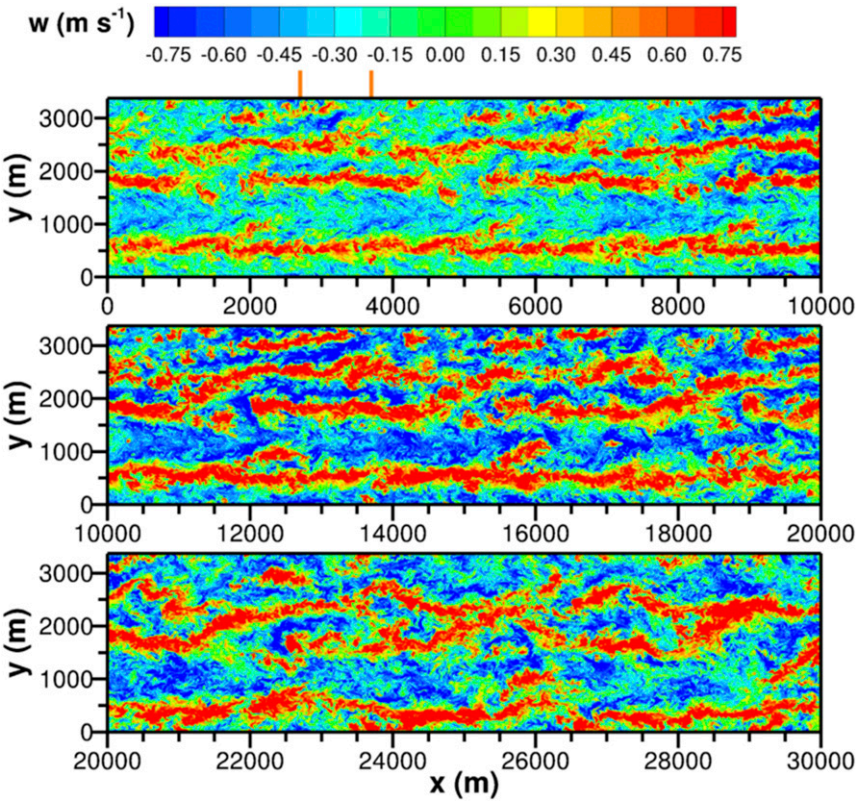

FIG. 6. Vertical velocity w as in Fig. 5, but in an x–y plane near the middle of the boundary layer at $z = 250$ m. Notice the increase in fluctuation intensity between $10\,000 < x < 20\,000$ m; also see Fig. 21.

extracted from the LES is shown here: we focus on vertical velocity because of its key role in boundary layer dynamics. Typical visualizations of $w(x, y)$ at $z = (50, 250, 500)$ m from simulation Eu2 are presented in Figs. 5–7, and at $z = (50, 250)$ m from simulation Es2 in Figs. 8 and 9. At a given z level the full horizontal domain is shown but for clarity it is split into three separate panels. The orange vertical lines in the upper panel of each figure depict the locations $(x_b, x_b + \ell)$ corresponding to the (start, end) of the SST jump; recall $x = 0$ is the right edge of the fringe region (Fig. 1). For each simulation, the color bar is held constant across the different z levels, and thus the w patterns can be fairly compared; notice the color bar range differs between simulations Eu2 and Es2. The images are typical w patterns in the simulations at late time $t > 2$ hr.

In the interior of the MABL, coherent elongated streaky structures are pervasive in these weakly unstable heterogeneous boundary-layers. The structures in the P domain propagate into the H domain at the left boundary $x = 0$ and are then advected over the heterogeneous SST. The structures are long-lived in time and space, meander in the x–y plane and often merge downstream, and are sensitive to the sign of the underlying SST jump. In the case $\Delta\theta > 0$, the structures intensify and broaden in y with increasing z, and at the top of the MABL break up and evolve into circular plumes. Because of horizontal advection, the streaks in the MABL "feel" the upstream change in SST at progressively greater downstream distances with increasing z. For example, in simulation Eu2 enhanced w fluctuations are first observed at $x > 6$ km for $z = 50$ m and at $x > 10$ km for $z = 250$ m. Near the top of the MABL, enhanced plumes appear at $x > 12$ km (Fig. 7). Close examination of the images at $z = 250$ m also shows an unexpected result, the intensity of the vertical fluctuations reaches a maximum in the intermediate range $10 < x < 20$ km, which leads to a local maximum in vertical velocity variance; see section 6e.

In simulation Es2 with a warm-to-cold change in SST the decay of the shear–convective streaks and evolution toward stably stratified turbulence is spatially protracted. The collapse of the w fluctuations is also biased, inspection of the figures shows downdrafts are quenched more rapidly than updrafts, see middle panels of Figs. 8 and 9. At $x > 22$ km only faint remnants of the streaks are present as the vertical velocity evolves toward small-scale stratified turbulence. And above $z > 250$ m, which is well below the upstream boundary layer depth $\widehat{z}_i \sim 560$ m, the residual turbulence is very weak (not shown).

b. *Surface-layer statistics*

SST variability impacts surface-layer variables (u_*, Q_*) downstream of warm and cold fronts. In large-scale models, these variables are estimated with bulk parameterizations

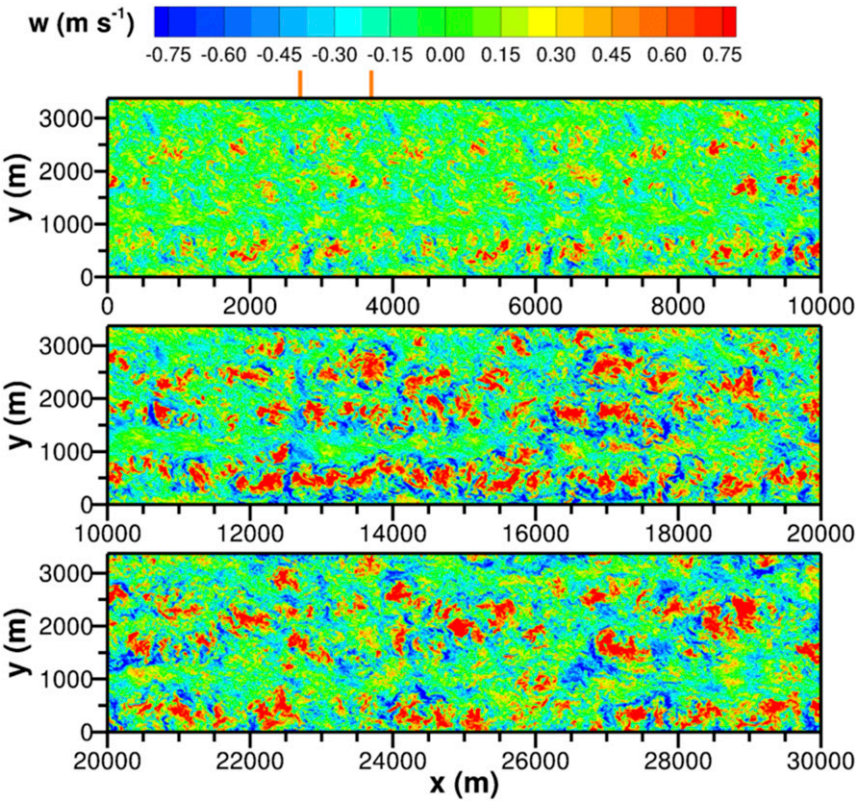

FIG. 7. Vertical velocity w as in Fig. 5, but in an x–y plane near the entrainment zone $z = 500$ m.

$$\boldsymbol{\tau} = -c_d|\Delta\mathbf{U}|\Delta\mathbf{U}, \tag{8a}$$

$$Q_* = -c_h|\Delta\mathbf{U}|(\Theta - \theta_s), \tag{8b}$$

based on winds and temperature fields ($\Delta\mathbf{U}$, Θ) located in the surface layer, most often $z = 10$ m (e.g., Fairall et al. 2003). The wind stress magnitude $u_*^2 = |\boldsymbol{\tau}|$, ($c_d$, c_h) are surface exchange coefficients, and $\Delta\mathbf{U}$ is the vector difference between the wind and surface drift current in the water.

LES estimates of $\langle u_*, Q_*\rangle$, essentially the left-hand side of (8), are depicted in Fig. 10. For reference, the bottom panel of this figure also shows the downstream SST variation $\delta\theta_s(x) = \theta_s(x) - \theta_o$. A first impression of the results is that $\langle Q_*\rangle(x)$ closely tracks $\delta\theta_s(x)$ for all combinations of ($\Delta\theta$, ℓ). This tight correlation can be interpreted based on (8b): if x variations in the exchange coefficient c_h and surface wind speed $|\Delta\mathbf{U}|$ are relatively slow then the response of the temperature flux Q_* tracks the SST boundary condition $\theta_s(x)$. The variation of the 10 m temperature also roughly tracks $\theta_s(x)$. Figure 10 shows this interpretation is applicable for both warm-to-warmer and warm-to-cold transitions. Closer examination of Fig. 10 also indicates that the variation of $\langle u_*\rangle(x)$ is spatially delayed relative to $\delta\theta_s(x)$. The lag is especially apparent when the temperature gradient is sharp, for example, in case Eu1 where $\ell = 100$ m, $\widehat{u_*}$ tends to an equilibrium value at a distance greater than 3 km downstream of the jump location, that is, the transition length scale $\delta x/\ell > 30$, where $\delta x = x - (x_b + \ell)$; in case Eu3 with $\ell = 3000$ m and $\delta x/\ell \sim 3.8$. The delayed spatial evolution of u_* compared to Q_* is a direct consequence of the thermal surface boundary condition. Perturbations in SST are felt immediately by the surface temperature flux but the internal couplings between the temperature and wind fields are slow by comparison resulting in a delayed response in the wind stress $\boldsymbol{\tau}$ to varying SST. However, if the heterogeneity is caused by changes in surface roughness, we speculate a rapid momentum response (Lin et al. 1997). Stratification, either unstable or stable, resulting from an SST jump plays an important role in how rapidly (u_*, Q_*) approach equilibrium values. In the warm-to-cold transition the spatial evolution of u_* is especially delayed because of the regime transition from unstable to stable surface-layer turbulence. In case Es2, the far right edge of the H domain is more than 20 km downstream of the SST jump, $\delta x/\ell > 200$, and $\langle u_*\rangle$ has not yet reached an asymptotic equilibrium value. For very sharp SST gradients, there are edge effects, small overshoots in $\langle u_*, Q_*\rangle$, similar to those found in simulations of highly convective turbulent flow over narrow Arctic leads (e.g., Lüpkes et al. 2008; Tetzlaff et al. 2015). In the present simulations with $0.1 < \ell < 6$ km and strong horizontal mean advection the adjustment in surface stress and temperature flux near fronts are correlated with changes in downward turbulent mixing, see section 6e. When advection is not dominant, the quasi-equilibrium of Samelson et al. (2006) predicts changes in surface wind stress are correlated with changes in boundary layer depth at large downstream distances, 50–500 km.

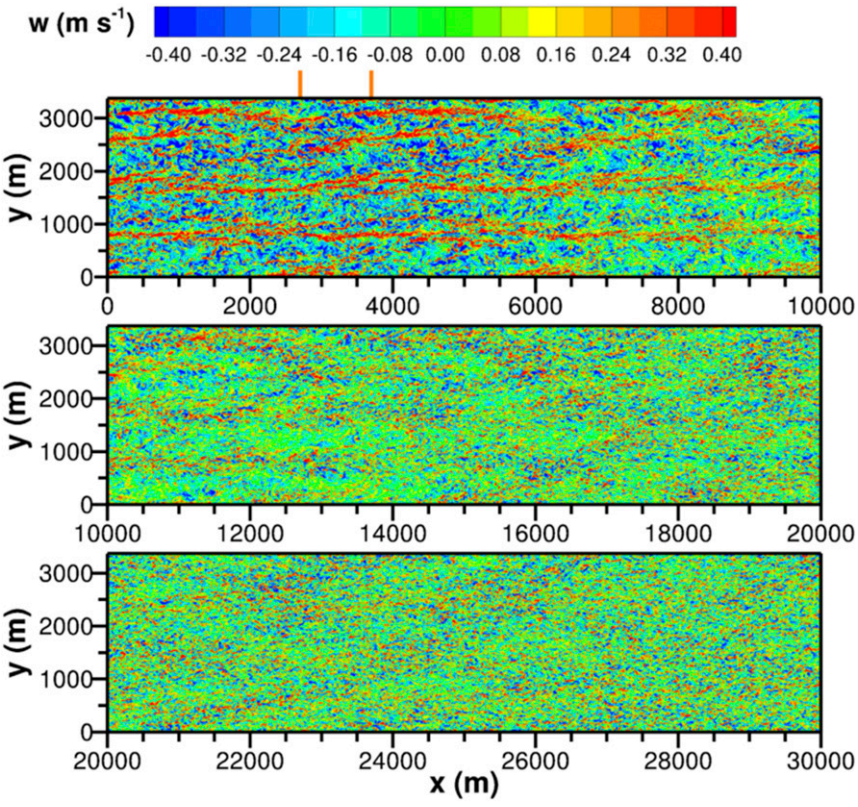

FIG. 8. Vertical velocity w in an x–y plane evolving over a cold SST jump in simulation Es2. The full H domain is depicted, but for visualization is split into three panels, each spanning 10 km of the domain. The x–y slice is near the surface layer at $z = 50$ m. (top) The orange vertical lines show the start and end of the SST jump $\Delta\theta = -1.5$ K spanning $\ell = 1000$ m. The color bar range is reduced compared to that shown in Fig. 5.

The dependence of friction velocity on SST variability is also reflected in gradients of the wind stress, namely, the divergence and curl $\langle \nabla \cdot \boldsymbol{\tau}, \nabla \times \boldsymbol{\tau} \rangle$ shown in Fig. 11. These are key variables revealed by satellite altimetry (e.g., Chelton et al. 2004) and are often used to infer atmosphere–ocean coupling at large scales (e.g., Gill 1982; Spall 2007; O'Neill et al. 2010). For the sharp small-scale SST changes employed in the LES we also find a positive correlation between wind stress divergence and the sign and magnitude of the jump in SST, $\langle \nabla \cdot \boldsymbol{\tau} \rangle \uparrow$ as $\Delta\theta/\ell \uparrow$. However, the LES results also show there is an additional dependence on downstream distance. For example, with $\Delta\theta/\ell = 2$ K/3000 m the stress divergence increases from zero at $x_b = 2700$ m reaching a maximum near $x \sim 5500$ m then followed by a decrease back toward zero. In our idealized simulations, with a single one-sided jump in SST, the wind stress progression from its upstream to downstream values requires a maximum in its horizontal gradient somewhere in the transition region. At downstream distances past the maximum in $\langle \nabla \cdot \boldsymbol{\tau} \rangle$ the stress divergence must decrease as u_* approaches an equilibrium state. Notice $\nabla \cdot \boldsymbol{\tau}$ for unstable and stable SST jumps are of opposite sign but similar magnitude, which supports the approximate linear relationship between $\nabla \cdot \boldsymbol{\tau}$ and SST gradient often reported in the presence of large-scale heterogeneity (e.g., Chelton et al. 2004; Small et al. 2008; Gemmrich and Monahan 2018). There is small-scale variability in $\nabla \cdot \boldsymbol{\tau}$, with local peaks near the upstream edge for very sharp SST fronts. With geostrophic winds blowing across the SST isotherms, the wind stress curl is small but nonzero because of Ekman wind turning in the boundary layer interior.

c. *Internal boundary layers*

Horizontal advection of air across a surface discontinuity, a step change, induces growing internal boundary layers (IBLs), for example, Stull (1988, p. 596), Garratt (1992, p. 104), and Kaimal and Finnigan (1994, chapter 4). In our weakly convective MABL both mechanical and thermal IBLs are generated because of the couplings between winds and stratification. Figures 12 and 13 illustrate development of mechanical IBLs downstream of warm and cold jumps in SST; in these figures $\Delta\theta = (2, -1.5)$ K and $\ell = 1000$ m, similar results are found with the ℓ variations in Table 2. To highlight the SST impact on the winds, we present contours of the perturbation or secondary wind component $\langle u_p \rangle(x, z) = \langle u \rangle(x, z) - \langle \hat{u} \rangle_{xy}(z)$, where $\langle \hat{u} \rangle_{xy}$ is the mean wind profile in the P domain (Fig. 3). As expected, a (positive, negative) jump in SST induces a secondary (speedup, slowdown) of the surface-layer winds and

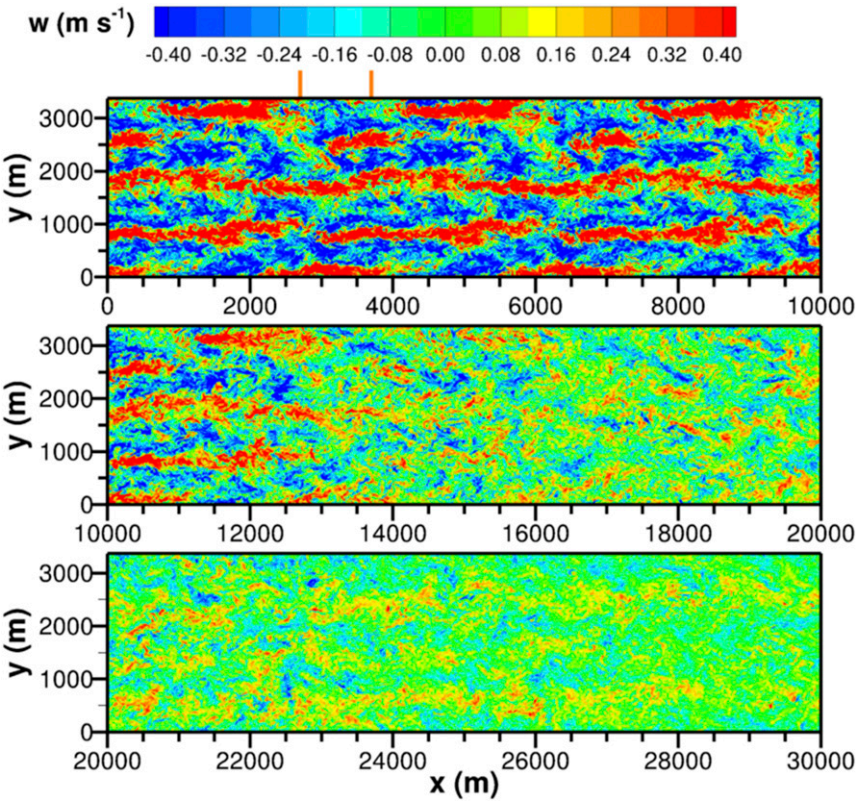

FIG. 9. Vertical velocity w as in Fig. 8, but in an x–y plane at $z = 250$ m.

secondary (negative, positive) return flow near the top of the boundary layer $\widehat{z}_i$. Also notice the response of the horizontal winds near the surface is earlier in x and stronger than their counterparts at the boundary layer top. In the boundary layer interior (downdrafts, updrafts) connect the secondary flows at the surface and boundary layer top for (warm, cold) SST jumps, respectively, see lower panels of Figs. 12 and 13. An unexpected feature is the x location of the w branches, more than 10 km downstream of the SST jump with a dependence on the sign of the SST jump. Because of surface heterogeneity average vertical velocity $\langle w \rangle(x, z) \neq 0$ in the boundary layer interior. With $\Delta\theta > 0$ the most negative downdraft region is concentrated in a thin zone near the top of the MABL at $x \sim 10$ km while $\Delta\theta < 0$ induces positive updrafts farther downstream $x \sim 20$ km near the top of a developing stable IBL. The peak magnitude $|\langle w \rangle| \sim 7\,\text{mm}\,\text{s}^{-1}$ in both cases is comparable to the entrainment velocity w_e in canonical horizontally homogeneous boundary layers.

The temperature field also develops thermal IBLs. This is illustrated in Figs. 14 and 15 where vertical profiles of mean temperature difference $\delta\theta = \langle \theta \rangle(x, z) - \theta_o$ are compared for simulations (Eu2, Es2) with (warm, cold) SST fronts, respectively. Profiles are shown at selected x locations upstream and downstream of the SST front. Observe at $x = 1350$ m the temperature profile upstream of the SST jump exhibits the classic shape for a horizontally homogeneous weakly convective shear boundary layer: $\langle \theta \rangle$ is well mixed over the bulk of the boundary layer with negative unstable gradients in the surface layer and positive stable gradients aloft, (e.g., see Moeng and Sullivan 1994; Fedorovich et al. 2004; Sullivan et al. 2014).

With $\Delta\theta > 0$ the temperature field in the surface layer, $z \leq 0.1\widehat{z}_i$, responds rapidly to the x variations in SST compared to its counterpart in the middle and upper layers of the MABL. For instance, at $x = 7000$ m and $z \geq 400$ m $\langle \theta \rangle \langle \theta \rangle(x, z) \simeq \langle \hat{\theta} \rangle_{xy}$ whereas in the surface layer $\langle \theta \rangle(x, z) \neq \langle \hat{\theta} \rangle_{xy}$ because of the SST variations. The rapid response of the surface-layer temperature is anticipated based on the variation of Q_* shown in Fig. 10. At a given x downstream of the SST jump, the MABL is then approximately divided into two vertical layers, the lower layer is a rapidly growing convectively unstable IBL that extends upward from the surface while the upper layer above the IBL is essentially the far upstream stratified flow independent of the SST heterogeneity. As a result of the vertical layering, the temperature profiles downstream of the SST jump feature a superadiabatic layer that extends from $z = 0$ well into the interior of the MABL, that is, $\langle \partial_z \theta \rangle < 0$ at z levels well above what is traditionally called the convective surface layer because of the growing IBL. The superadiabatic layer has significant impact on turbulence, entrainment, and the far downstream evolution of the flowfields, see section 6e. Only at $x > 20$ km does the θ profile take on a shape typical of a well-mixed layer.

A metric showing the impact of a positive jump in SST is the x–z distribution of mean vertical temperature gradient $\langle \partial_z \theta \rangle$ shown in the lower panel of Fig. 14. The color bar highlights the

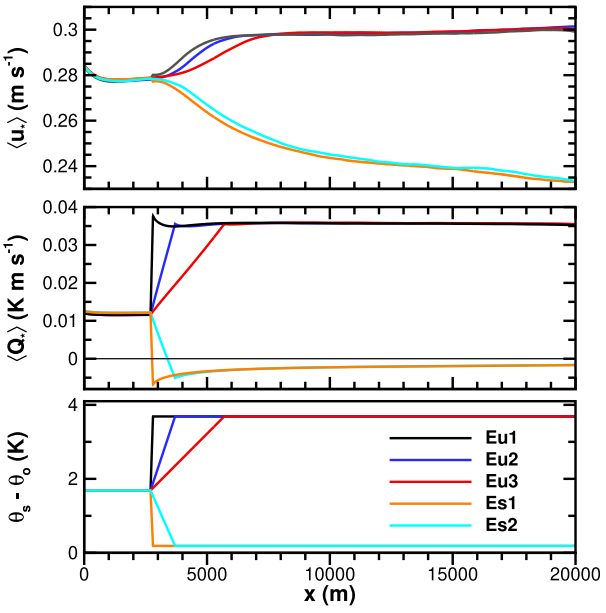

FIG. 10. Surface-layer variables (top) $\langle u_* \rangle$ and (middle) $\langle Q_* \rangle$ downstream of warm and cold SST fronts with (bottom) spatial distribution $\delta\theta_s(x) = \theta_s(x) - \theta_o$. The line colors and names in the bottom panel correspond to the simulations in Table 2.

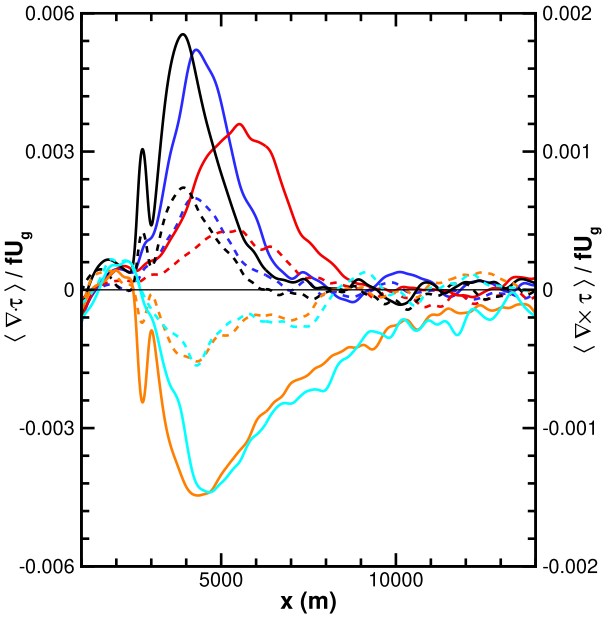

FIG. 11. Spatial evolution of the divergence and curl of the surface stress: $\langle \nabla \cdot \boldsymbol{\tau} \rangle$ (left vertical axis) and $\langle \nabla \times \boldsymbol{\tau} \rangle$ (right vertical axis) are indicated by solid and dashed lines, respectively. The variables are made dimensionless by fU_g. The SST gradient $\Delta\theta/\ell$ is 2 K/100 m, 2 K/1000 m, and 2 K/3000 m for the black, blue, and red colors respectively, and -1.5 K/100 m and -1.5 K/1000 m for the orange and cyan colors.

vertical level of neutral stratification in the interior of the MABL, that is, the level $z_n(x)$ where $\langle \partial_z \theta \rangle$ switches from mean unstable to mean stable stratification. The results in Fig. 14 are surprising, they show a nonmonotonic spatial variation of the temperature field in response to $\Delta\theta > 0$. Downstream of the SST jump z_n features a pronounced local maximum; z_n grows, peaks, and decays in the interval $5 < x < 15$ km where SST $\theta_s = \theta_c + \Delta\theta$ is constant. Hereafter the region where z_n peaks is referred to as a thermal overshoot. Inspection of the results shows the horizontal wind creates spatial asymmetry by tilting the temperature gradient contours in the downstream direction. The spatial variations in $\langle \partial_z \theta \rangle$ are unexpected, and prompted simulation Eu4 with a wider jump length $\ell = 6$ km. The spatial patterns of $\langle \theta \rangle$ and $\langle \partial_z \theta \rangle$ in Eu4 and Eu2 are similar but with the x location of the overshoot displaced farther downstream. The dynamics underlying the temperature overshoot in these weakly convective MABLs are coupled to the turbulence, namely, the vertical variance, vertical temperature flux, and the temperature variance as discussed in section 6e. Simulations of highly convective flow over Arctic leads of finite width sandwiched between upstream and downstream stable boundary layers also feature overshooting thermal plumes (Lüpkes et al. 2008). At large distances downstream of the front, $x > 15$ km, the MABL grows and z_n steadily increases over the LES domain.

In simulations with $\Delta\theta = -1.5$ K the developing IBL is cooled and the surface layer responds rapidly to $Q_* < 0$; the mean temperature gradient $\langle \partial_z \theta \rangle > 0$ at the surface. In the middle of the layer, say $z = 250$ m m, the transition of the temperature profile to a stable profile is smooth and $\langle \partial_z \theta \rangle > 0$ becomes more pronounced with increasing x as the turbulence in the interior of the MABL collapses. Overall, the MABL temperature and wind fields with positive and negative SST jumps remain in a spatially evolving state that extends far downstream from the SST jump. Broadly similar results are found with varying ℓ for the same jumps $\Delta\theta = (2, -1.5)$ K as in Figs. 12 and 13.

d. Temperature and momentum budgets

The mean temperature and momentum budgets expose important effects in turbulent flow over a heterogeneous water surface. Using the decomposition (6) in (1a) and (1b), the LES mean temperature budget and streamwise momentum budget read, respectively,

$$\underbrace{\partial_t \langle \theta_p \rangle}_{T} = \underbrace{-\langle u \rangle \partial_x \langle \theta \rangle}_{H_{\rm adv}} \underbrace{-\langle w \rangle \partial_z \langle \theta \rangle}_{V_{\rm adv}} \underbrace{-\partial_z \langle w'\theta' + \tau_{w\theta} \rangle}_{V_{\rm div}} \underbrace{-\partial_x \langle u'\theta' + \tau_{u\theta} \rangle}_{H_{\rm div}} \underbrace{-\partial_t \langle \hat{\theta} \rangle_{xy}}_{T_{\rm bak}}, \tag{9a}$$

$$\underbrace{\partial_t \langle u \rangle}_{T} = \underbrace{-\langle u \rangle \partial_x \langle u \rangle}_{H_{\rm adv}} \underbrace{-\langle w \rangle \partial_z \langle u \rangle}_{V_{\rm adv}} \underbrace{-\partial_z \langle u'w' + \tau_{uw} \rangle}_{V_{\rm div}} \underbrace{-\partial_x \langle u'u' + \tau_{uu} \rangle}_{H_{\rm div}} \underbrace{+f\langle v \rangle}_{C_{\rm or}} \underbrace{-\langle \partial_x p \rangle/\rho}_{P_{\rm grd}}, \tag{9b}$$

where $(\tau_{u\theta}, \tau_{w\theta})$ and (τ_{uu}, τ_{uw}) are SGS temperature and momentum fluxes. In left-to-right order the terms in (9) are time tendency T, mean (horizontal, vertical) advection ($H_{\rm adv}$, $V_{\rm adv}$),

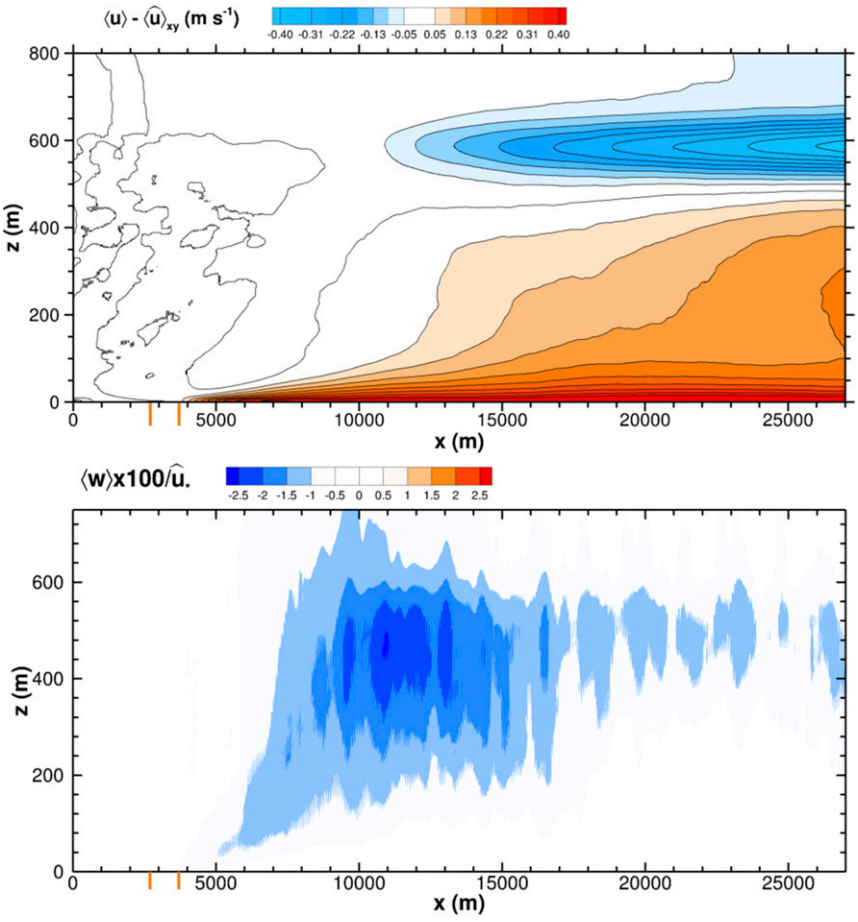

FIG. 12. (top) Perturbation velocity $\langle u_p \rangle(x, z) = \langle u \rangle(x, z) - \langle \hat{u} \rangle_{xy}(z)$ for a warm SST front $(\Delta\theta, \ell) = (2\,\mathrm{K}, 1000\,\mathrm{m})$. (bottom) Average vertical velocity $\langle w \rangle(x, z)$ normalized by $\widehat{u_*}$. The orange vertical lines at the bottom of the panels mark the start and end location of the SST front. The mean wind profile in the P domain $\langle \hat{u} \rangle_{xy}(z)$ is shown in Fig. 3.

mean (vertical, horizontal) turbulence flux divergence (V_{div}, H_{div}), and in the momentum budget (Coriolis force, horizontal pressure gradient) (C_{or}, P_{grd}), respectively. To account for continual heating in the upstream inflow time tendency in the temperature budget (9a) is split using the decomposition $\langle \theta \rangle = \langle \theta_p \rangle + \langle \hat{\theta} \rangle_{xy}$; $\langle \theta_p \rangle$ is the perturbation temperature over the heterogeneous domain. In the homogeneous upstream flow $\partial_t \langle \hat{\theta} \rangle_{xy} = -\partial_z \langle \widehat{w'\theta'} + \widehat{\tau_{w\theta}} \rangle_{xy} \equiv T_{\mathrm{bak}}$ and is constant in the MABL interior.

The streamwise variation of the mean temperature budget, (9a), at three vertical levels is depicted in Figs. 16 and 17 for cases Eu2 and Es2, respectively. The orange line in Figs. 16 and 17 is the sum of all terms on the right-hand side of (9a), that is, the time tendency residual $T \approx 0$ and the mean temperature budget is nearly closed. Inspection of the results shows a balance at all x and z between three terms, namely, $T_{\mathrm{bak}} + H_{\mathrm{adv}} + V_{\mathrm{div}}$. Terms V_{adv} and H_{div} are are not presented. These terms are small in the bulk of the layer where $\langle w \rangle < \langle u \rangle$, $\partial_z \langle \theta \rangle \approx 0$, and the (horizontal, vertical) length scales are (large, small) so that $\partial_x \langle u'\theta' \rangle < \partial_z \langle w'\theta' \rangle$ (Wyngaard 2010).

The results illustrate the evolving spatial balance between horizontal advection and vertical flux divergence. In the case with $\Delta\theta > 0$, $H_{\mathrm{adv}} < 0$ over the full depth of the boundary layer and remains finite even at large x distances where $\langle Q_* \rangle$ is nearly constant: note $H_{\mathrm{adv}} < 0$ implies $\langle \partial_x \theta \rangle > 0$. At a given z level, as x varies vertical flux divergence induced by the jump in surface heating is balanced by mean horizontal advection and T_{bak} not by local time tendency T.

The temperature perturbation decays vertically but is spread over the full boundary layer. In the surface layer and also in the entrainment zone V_{div} and $-H_{\mathrm{adv}}$ feature compensating local maximums with the x location of the extrema increasing with increasing z. For instance, at $z = 20\,\mathrm{m}$ V_{div} peaks at $x \sim 4\,\mathrm{km}$ and at $z = 450\,\mathrm{m}$ peaks at $x \sim 12\,\mathrm{km}$ well downstream of the SST jump $x_b + \ell = 3.37\,\mathrm{km}$. Also, there is a noticeable leveling off of the flux divergence in the surface layer between $6 < x < 11\,\mathrm{km}$, which appears connected to the location of maximum overshoot in temperature (Fig. 14).

A transition from unstable to stable turbulence is reflected in the temperature budget shown in Fig. 17 with $\Delta\theta < 0$.

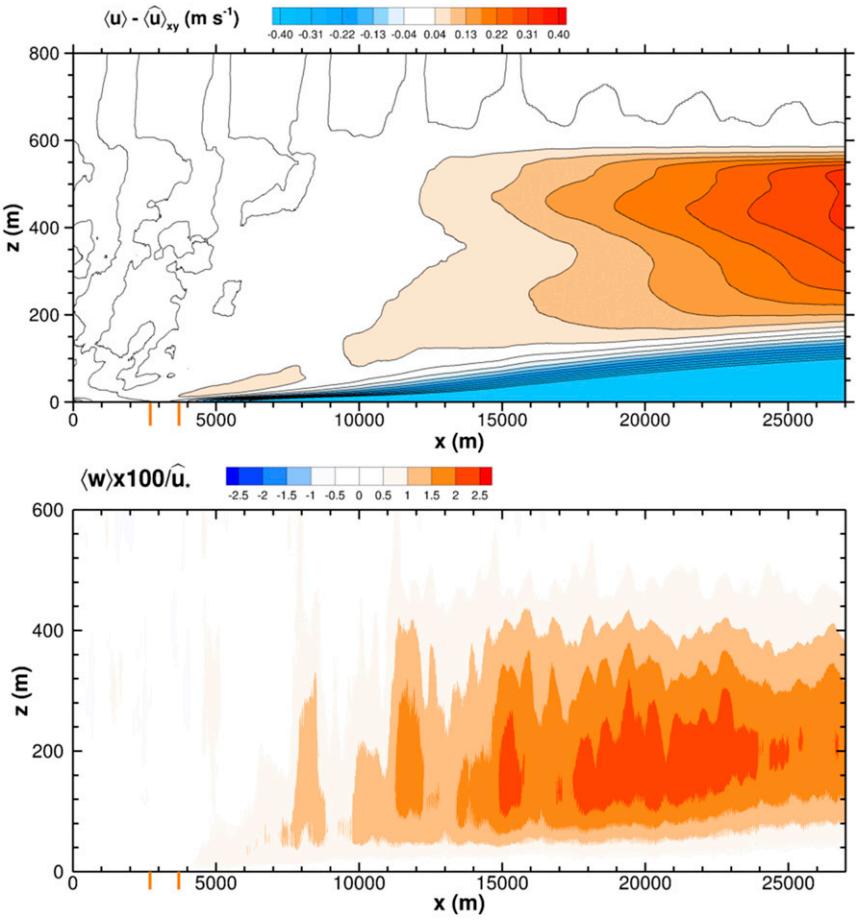

FIG. 13. (top) Perturbation velocity $\langle u_p \rangle(x, z) = \langle u \rangle(x, z) - \langle \hat{u} \rangle_{xy}(z)$ for a cold SST front $(\Delta\theta, \ell) = (-1.5\,\mathrm{K}, 1000\,\mathrm{m})$. (bottom) Average vertical velocity $\langle w \rangle(x, z)$ normalized by $\widehat{u_*}$. The orange vertical lines at the bottom of the panels mark the start and end location of the SST front. The mean wind profile in the P domain $\langle \hat{u} \rangle_{xy}(z)$ is shown in Fig. 3.

Notice the sign switch at lower heights, $V_{\mathrm{div}} < 0$, $H_{\mathrm{adv}} > 0$, as the flow passes over the jump in SST jump. Also, H_{adv} is nonzero at large x but with low levels of turbulence and small vertical flux divergence $H_{\mathrm{adv}} > 0$ primarily serves to balance $T_{\mathrm{bak}} < 0$; this is readily observed at $z > 50$ m where the stably stratified turbulence is weak.

The x variation of the mean streamwise momentum budget (9b) at four vertical levels $z = (20, 250, 450, 600)$ m is depicted in Fig. 18 for case Eu2. Inspection of the results shows a primary balance at all x and z between four terms, namely, $H_{\mathrm{adv}} + V_{\mathrm{div}} + P_{\mathrm{grd}} + C_{\mathrm{or}}$. Terms V_{adv} and H_{div} are small and are not shown. Over the time period of the analysis 5400 s, the Coriolis term is nearly constant with x, as the wind turning with height is nearly independent of the SST jump, while the streamwise pressure gradient has a modest x maximum close to the surface that decays with increasing z. In the entrainment zone, $P_{\mathrm{grd}} \approx 0$. Horizontal advection (red curve in Fig. 18) is interesting, it displays a sign change matching the secondary circulations in Fig. 12. Near the surface $H_{\mathrm{adv}} < 0$, $\langle \partial_x u \rangle > 0$, as the wind speed increases passing over a positive SST jump. Horizontal advection reverses sign in the entrainment zone $H_{\mathrm{adv}} > 0$, $\langle \partial_x u \rangle < 0$. Enhanced turbulence downstream of the SST jump induces growth of the boundary layer and as a result the winds near $\langle z_i \rangle$ decrease.

In these heterogeneous MABLs with single-sided fronts the far downstream temperature and momentum budgets contain finite horizontal advection. At large x, the MABL is, however, analogous to a spatially homogeneous boundary layers but with a different upstream history of deepening, see section 6f.

e. *Fluxes and variances*

The streamwise extent of domain H is nearly $50\widehat{z_i}$, which allows an examination of turbulence in x regions close to and far from the SST jump over the full depth of the MABL. One of the unexpected findings from our analysis is a nonmonotonic evolution of the turbulence statistics in the interior of the MABL with $\Delta\theta > 0$. This is hinted at based on the mean flow patterns discussed previously. The x–z variation of turbulent temperature flux $\langle w'\theta' \rangle$ for simulation Eu2 shown in Figs. 19 illustrates the complex spatial evolution of turbulence (see Fig. 21 below for the x–z variation of vertical velocity variance $\langle w'^2 \rangle$ for simulation Eu2). In Fig. 19 contours of resolved

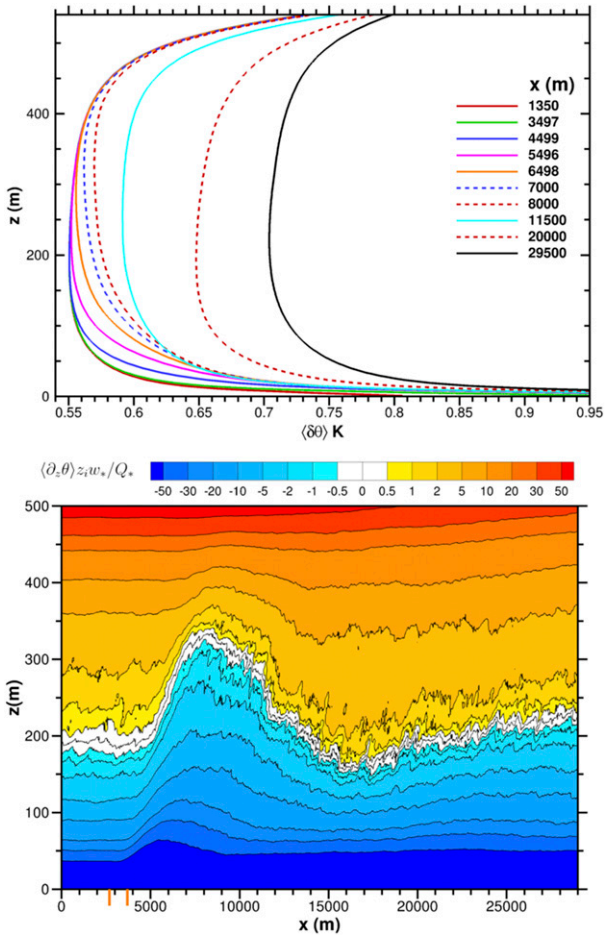

FIG. 14. (top) Vertical profiles of the temperature difference $\langle \delta\theta \rangle = \langle \theta - \theta_o \rangle$ at selected x locations for a warm SST front, case Eu2. (bottom) Contours of vertical temperature gradient $\langle \partial_z \theta \rangle$ normalized by $\widehat{Q_*}/\widehat{z_i}\widehat{w_*}$. Notice the overshoot and the vertical location where the gradient changes sign indicated by the band of white colors in the bottom panel.

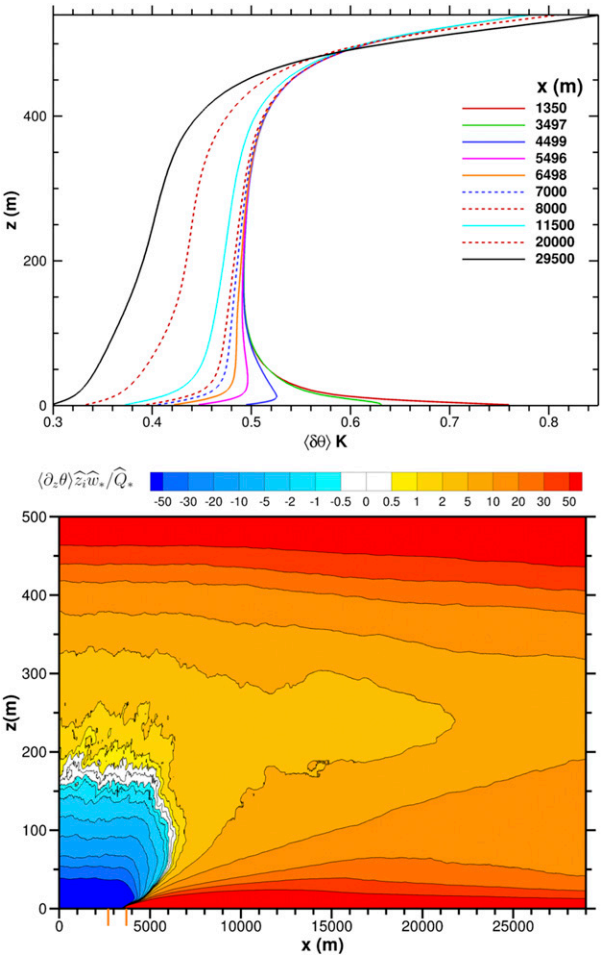

FIG. 15. (top) Vertical profiles of the temperature difference $\langle \delta\theta \rangle = \langle \theta - \theta_o \rangle$ at selected x locations for a cold SST front, case Es2. (bottom) Contours of vertical temperature gradient $\langle \partial_z \theta \rangle$ normalized by $\widehat{Q_*}/\widehat{z_i}\widehat{w_*}$.

temperature flux $\langle w'\theta' \rangle$ are depicted in the top panel while the bottom panel shows vertical profiles of total (resolved plus SGS) temperature flux at selected x locations. To reduce the random variability the vertical profiles are further smoothed over a running x interval of width 1000 m in addition to the y–t.

Similar to $\langle \partial_z \theta \rangle$ the temperature flux contours feature a nonmonotonic x–z spatial variation. The z location of a constant flux contour, for example, $\langle w'\theta' \rangle / \widehat{Q_*} = 1$, grows rapidly, reaches a maximum, and then falls in the interval $x = [3.3\text{–}19]$ km. After the descent, the height of an individual flux contour smoothly grows for $x > 19$ km. The vertical profile of temperature flux in the lower panel of Fig. 19 features a flux maximum in mid-MABL near $x \sim 11.5$ km. At this x location, the flux profile is nonlinear in z and overshoots the linear flux profile far downstream at $x = 29.5$ km over the full vertical extent of the MABL. Also, an increase in entrainment flux at $x \sim 11.5$ km is observed. In the interval $3.3 < x < 11.5$ km where the thermal IBL is growing, the temperature flux profile is a compound curve composed of two segments. In the lower MABL, the flux profile matches the local surface flux $\langle Q_* \rangle(x)$ and exhibits a sharp concave upward shape with increasing z. This curved lower profile blends smoothly into the far upstream linear profile at interior z locations, with the height of the matching points increasing with x.

In our weakly convective boundary layer, Eu2, we empirically estimate the thermal IBL depth $z_{\rm ibl}$ at each x location based on a simple flux matching rule; that is, $z_{\rm ibl}$ is the first z location from the surface that satisfies

$$\langle w'\theta' \rangle(x, z) = \widehat{\langle w'\theta' \rangle}_{xy}(z). \tag{10}$$

Based on (10), adopting a matching tolerance of 2%, we find the IBL depth $z_{\rm ibl}$ grows linearly with x but only up to the vertical location where $\widehat{\langle w'\theta' \rangle}_{xy}(z) = 0$. In other words, the vertical growth of the IBL is blocked by its first encounter with the entrainment zone. In Fig. 19, the temperature flux profile switches sign at approximately $z_{\rm ibl} = 0.8\widehat{z_i} = 400$ m, which

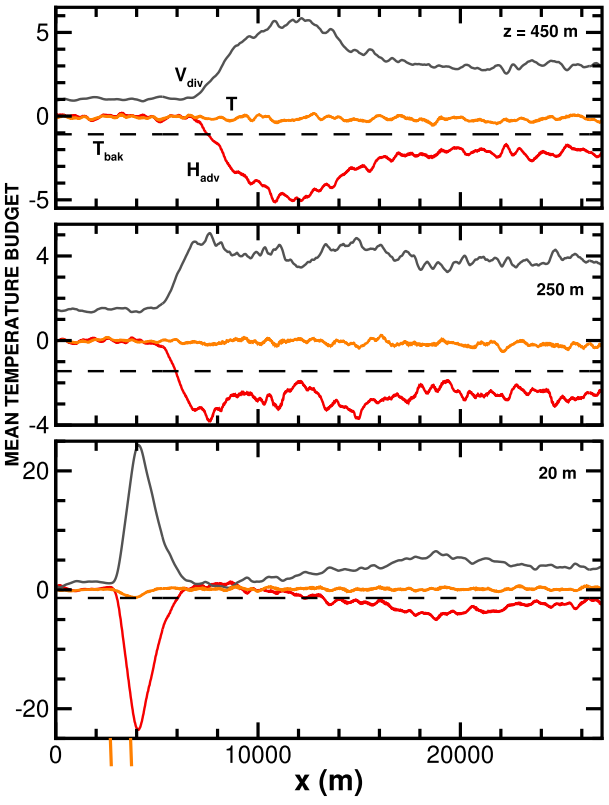

FIG. 16. Streamwise variation of terms in the mean temperature budget at z = (bottom) 20, (middle) 250, and (top) 450 m for simulation Eu2. The principal terms in (9a), i.e., $T_{\rm bak}$, $H_{\rm adv}$, $V_{\rm div}$, and T, are denoted by black dashed, red solid, black solid, and orange solid lines, respectively. The range of the vertical axis changes between the panels and terms are normalized by $\widehat{Q}_*/\widehat{z}_i$. The orange vertical lines in the bottom panel mark the start and end location of the SST front.

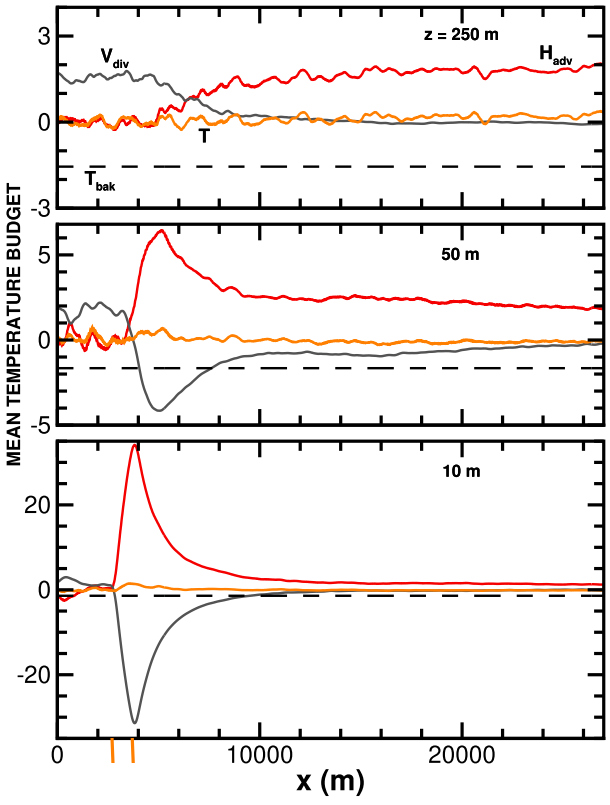

FIG. 17. Streamwise variation of terms in the mean temperature budget at z = (bottom) 10, (middle) 50, and (top) 250 m for simulation Es2. The labeling is as in Fig. 16.

occurs at the downstream location $x \approx x_b + 3.8$ km. When the growing IBL reaches the entrainment zone, unstable convective turbulence generated by the SST jump first interacts with stably stratified turbulence in the boundary layer inversion. Then the interior and surface layer of the MABL are fully coupled. However, the boundary layer is in disequilibrium and undergoes a spatial transition as the turbulence adjusts to the upstream SST perturbation. At downstream distances $x >$ 19 km, the vertical profile of temperature flux is linear in z with a weak x dependence. Based on this metric the turbulence is near equilibrium (section 6f).

In case Es2 with a warm-to-cool transition the temperature flux at $x < 10$ km displays vertical layers of unstable and stably stratified turbulence as the flow advects over the cold SST front (Fig. 20). Near the surface the temperature flux rapidly adjusts to the surface cooling while the transition in the upper layers $z > 200$ m is slow by comparison where the turbulence remains convectively unstable. Notice, similar to Eu2, the temperature flux exhibits a nonmonotonic transition with x. For $x \sim 10.5$ km the temperature flux is negative over the full depth of the boundary layer $0 < z < \widehat{z}_i$. Farther downstream at $x \sim 20$ km, stably stratified turbulence is mainly confined to levels $z <$ 200 m based on the first zero-crossing of the temperature flux profile. There is residual weakly decaying turbulence between 200 m $< z < \widehat{z}_i$.

Contours of vertical velocity variance for Eu2 and Es2 further illustrate the nonmonotonic spatial evolution of turbulence (Fig. 21). In the simulation with a warm front the variance has a prominent maximum in the middle of the boundary layer at $x \sim 13$ km; notice the peak is slightly downstream of the location of the temperature flux overshoot in Fig. 19. Inspection of the variance contours and vertical profiles downstream of this local maximum show that the middle and upper layers of the boundary layer remain in a spatially evolving state far downstream of the SST front. In the outer layer the turbulence time scale $T_t = z_i/w_* \sim 630$ s is long and coupled with the fast winds $\langle u \rangle \sim 10\ {\rm m\ s^{-1}}$ the horizontal distance required for turbulence to reach an equilibrium state, say $10\langle u \rangle T_t$, exceeds the horizontal extent of domain H. Case Es2 features a decaying mid-MABL maximum overlying surface-layer turbulence that is rapidly adjusting to the change in surface forcing.

f. *Lagrangian advection of thermal air parcels*

Horizontal advection in the mean temperature budget, and also the momentum budget, is nonzero at large x distances downstream of an SST jump, for example, $\langle u \rangle \partial_x \langle \theta \rangle > 0$

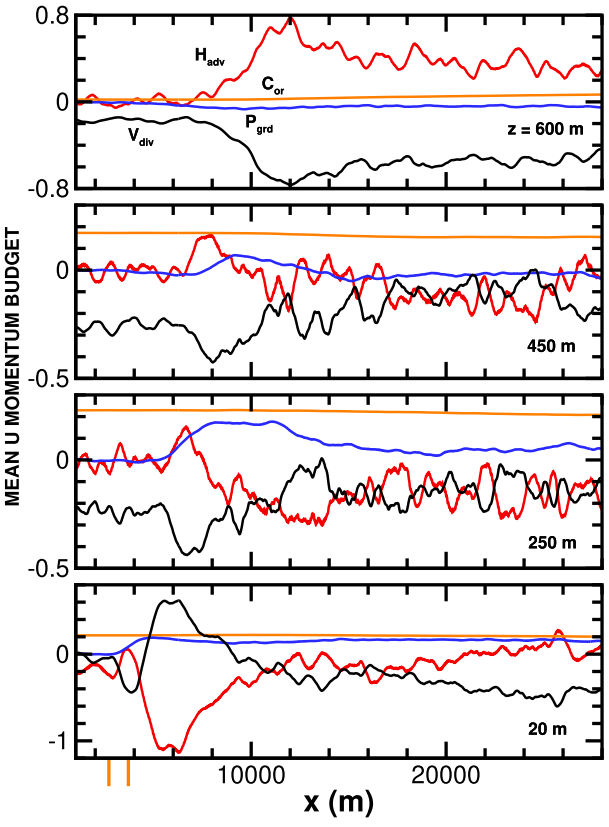

FIG. 18. Streamwise variation of terms in the mean momentum budget at (bottom to top) $z = 20, 250, 450$, and 600 m for simulation Eu2. The principal terms in (9b), i.e., H_{adv}, V_{div}, C_{or}, and P_{grd}, are denoted by red, black, orange, and blue lines, respectively. The range of the vertical axis changes between the panels and terms is normalized by $\widehat{u_*}/\widehat{z_i}$. The orange vertical lines in the bottom panel mark the start and end location of the SST front.

at $x > 20$ km at all z levels in Fig. 16. This is unexpected and raises an important query: How does an MABL with a single-sided surface temperature front approach a horizontally homogeneous state? Because of entrainment the stratified MABL is inherently unsteady and its spatial evolution above surface heterogeneity differs from a developing neutral boundary layer bounded between solid walls as in internal flows, that is, pipe or channel flows.

To fix ideas, consider the mean temperature budget written in terms of Lagrangian advection of air parcels, (9a) applies equally for heterogeneous and homogeneous boundary layers. At large x or long time t Lagrangian advection is then solely balanced by vertical divergence of total turbulent temperature flux:

$$\frac{D\langle\theta\rangle}{Dt} = \frac{D\langle\theta\rangle_{\text{hom}}}{Dt} = -\frac{\partial}{\partial z}\langle w'\theta' + \tau_{w\theta}\rangle, \tag{11}$$

or, equivalently,

$$\partial_t\langle\theta\rangle + \langle u\rangle\partial_x\langle\theta\rangle = \partial_t\langle\theta\rangle_{\text{hom}} = -\frac{\partial}{\partial z}\langle w'\theta' + \tau_{w\theta}\rangle. \tag{12}$$

In (11), $\langle\theta\rangle_{\text{hom}}$ is the temperature field under horizontally homogeneous conditions $\partial_x\langle\theta\rangle_{\text{hom}} \equiv 0$.

Motivated by (12), we can then estimate the left-hand sides of (12) by comparing the spatial evolution of average vertical flux $\langle w'\theta'\rangle(x, z)$ from the heterogeneous simulation Eu2 with the temporal evolution of average vertical flux $\langle w'\theta'\rangle(t, z)$ from a comparably forced homogeneous simulation Ehom. The SST in Ehom is constant in time and uniform in space $\theta_s = \theta_c + \Delta\theta$, with $\Delta\theta = 2$ K, and is specifically chosen to match the surface forcing in Eu2 at large x. Further, to create a fair comparison Ehom also utilizes the same restart volume with fully developed turbulence as used to start Eu2. The simulation details of Ehom are otherwise identical to those in the P domain previously described in section 4.

A (t–z) Hovmöller diagram of the resolved temperature flux from Ehom normalized by $\widehat{Q_*}$ is shown in Fig. 22 and is to be compared with the (x–z) diagram of temperature flux from Eu2 in Fig. 19. For reference the upper abscissa in Fig. 22 is an average Lagrangian distance $X = Ut$ assuming a constant mixed layer wind $U = 8.6\,\text{m s}^{-1}$. The temperature flux in Ehom at each time is constructed by averaging over its full x–y domain with a slight running time average to further smooth the contours.

As anticipated the temperature flux from Eu2 and Ehom differ markedly at small t or small x, as Ehom does not contain the pronounced temperature flux overshoot and decay that is a marked feature of Eu2. Also, the early evolution of the entrainment zones differ noticeably between the two simulations with Ehom deepening more quickly. Near a surface front time and distance are then not interchangeable and a homogeneous simulation with time varying surface forcing is not adequate to capture the boundary layer dynamics with spatial heterogeneity as found in Eu2. Horizontal advection is nonzero and important in the mean temperature budget over a heterogeneous surface.

To make a quantitative comparison between the temperature fluxes from Ehom and Eu2 at long t or large x we choose time and space locations, respectively, where the average boundary layer depth $\langle z_i\rangle$ from the two simulations match, this requires averaging. In Eu2 between $x = [27.3–28.2]$ km average $\langle z_i\rangle = 615$ m and in Ehom over the time period $t = [3500–6500]$ s average $\langle z_i\rangle = 647$ m. Average vertical profiles of total temperature and momentum fluxes and resolved velocity variances from Eu2 and Ehom at these space and time locations are compared in the lower panel of Fig. 22. To account for the small differences in (Q_*, u_*^2, z_i) each simulation uses their particular values of these quantities for normalization. The temperature flux agreement is excellent while the agreement between the momentum fluxes and velocity variances is also quite good as is the agreement between the mean wind and temperature profiles (not shown); the discrepancies are within the sampling errors from the two simulations.

Thus, at large distances downstream from a single-sided SST front simulation Eu2 produces boundary layer wind and temperature fields that match those from a similarly forced spatially homogeneous simulation. However, in the MABL flowing over a heterogeneous surface horizontal advection is

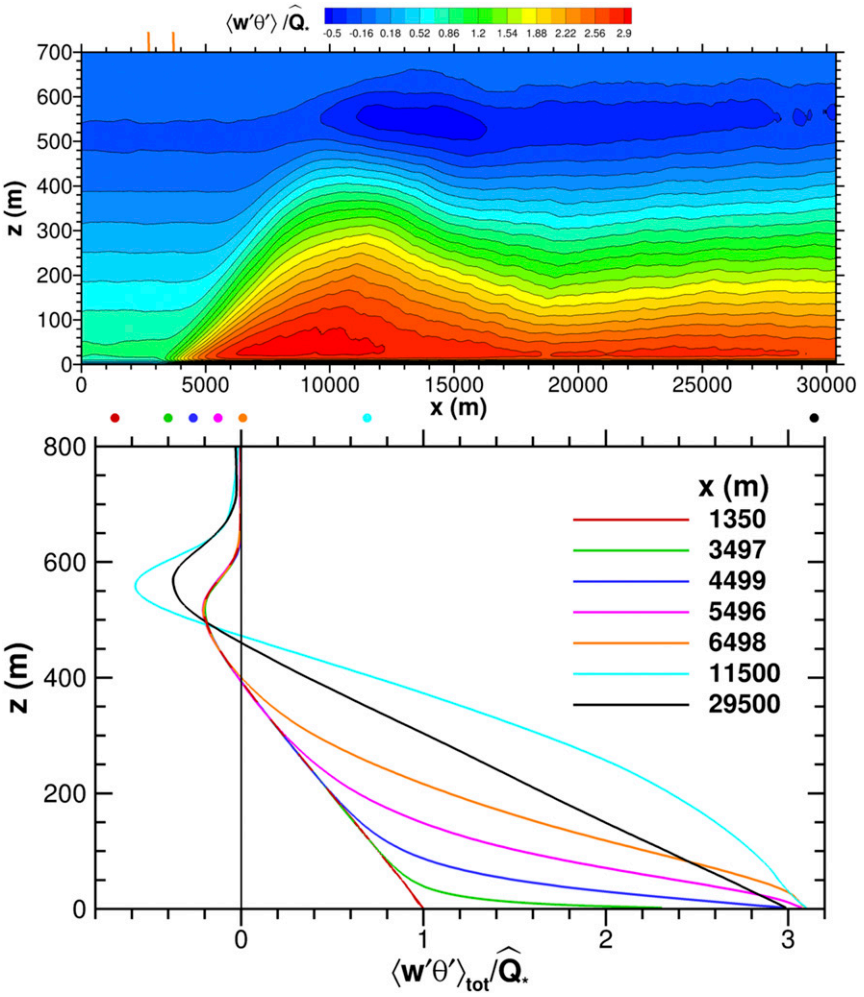

FIG. 19. (top) Contours of resolved temperature flux and (bottom) vertical profiles of total temperature flux (resolved plus SGS) for turbulent flow over an unstable SST front. The fluxes are normalized by $\widehat{Q}_*$ and the vertical profiles are shown at different x locations downstream of the SST front. The colored bullets in the top panel indicate the x location of the vertical profiles in the bottom panel. For comparison with results with homogeneous SST, see Fig. 22.

nonzero at large downstream distances and again acts to balance the vertical divergence of turbulent fluxes.

g. *Thermal overshoot and entrainment with positive SST jumps*

To guide the interpretation of the thermal overshoot found in Fig. 14 we next examine the primary production terms in the resolved-scale prognostic rate equations for temperature flux $\langle w'\theta'\rangle$ and variance $\langle \theta'^2\rangle$:

$$\partial_t\langle w'\theta'\rangle + \langle u\rangle\partial_x\langle w'\theta'\rangle = \underbrace{-\langle w'^2\rangle\partial_z\langle\theta\rangle}_{M} \underbrace{+\beta\langle\theta'^2\rangle}_{B} + \cdots \quad \text{(13a)}$$

$$\partial_t\langle\theta'^2\rangle + \langle u\rangle\partial_x\langle\theta'^2\rangle = \underbrace{-2\langle w'\theta'\rangle\partial_z\langle\theta\rangle}_{M} + \cdots \quad \text{(13b)}$$

In (13) the left-hand-side terms are time tendency and horizontal advection, the right-hand side of (13a) contains mean M and buoyancy (temperature variance) B production terms, and the right-hand side of (13b) is mean production by temperature flux. The ellipses in (13) denote all the numerous remaining terms in the full budgets documented in Stull (1988, chapter 4): SGS contributions to the budgets are ignored. Production of temperature flux by buoyancy B is positive while the sign of the mean production M depends on the product of vertical velocity variance and mean vertical temperature gradient, see Fig. 21 and the bottom panel of Fig. 14, respectively. In particular the sign and magnitude of M depends on the spatial overlap between $\langle w'^2\rangle$ and $-\langle\partial_z\theta\rangle$.

The sum of the production terms $P = M + B$ for varying x and z is shown in Fig. 23. In the lower MABL, $P > 0$ and is a significant source of positive temperature flux as expected. The

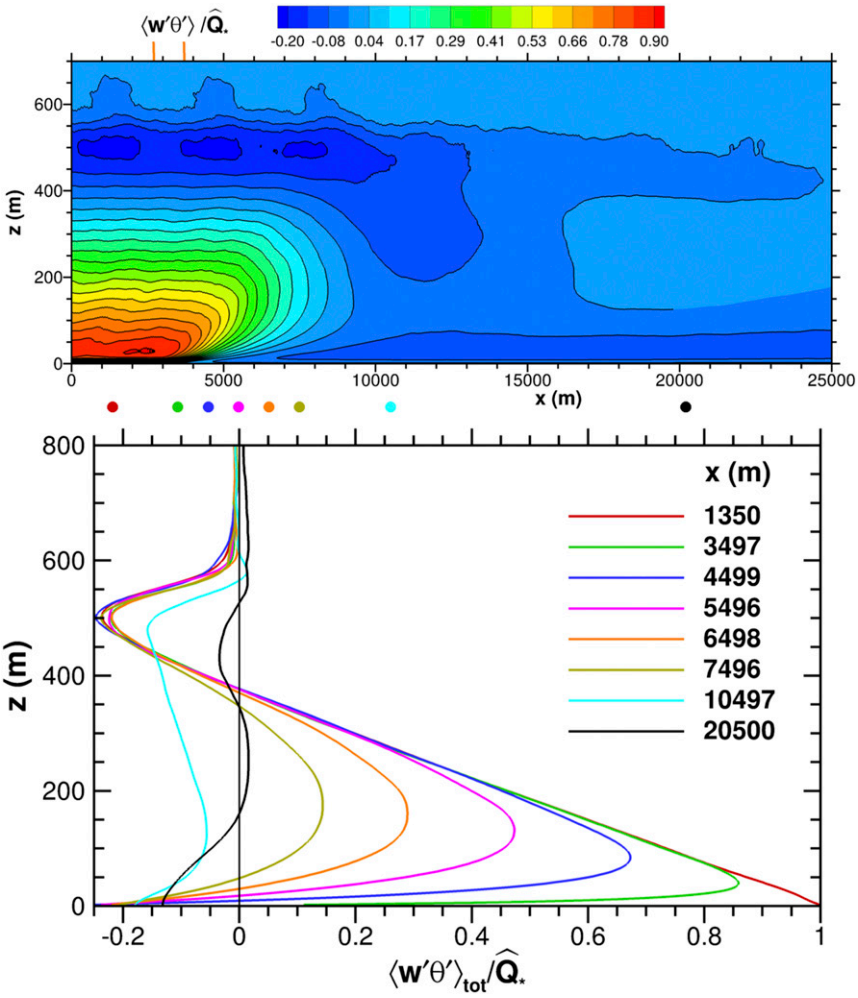

FIG. 20. (top) Contours of temperature flux and (bottom) vertical profiles of total temperature flux (resolved plus SGS) for turbulent flow over a stable SST front $\Delta\theta/\ell = -1.5\,\mathrm{K}/1000\,\mathrm{m}$. The fluxes are normalized by $\widehat{Q_*}$ and the vertical profiles are shown at different x locations downstream of the SST front. The colored bullets in the top panel indicate the x location of the vertical profiles in the bottom panel.

key feature of Fig. 23, however, is the sign switch of P in the upper layers of the MABL. Notice near $x \sim 12\,\mathrm{km}$ just above the thermal overshoot in Fig. 14, there is a closed set of negative contours featuring quite strong negative temperature flux production. Total $P < 0$ results from a sign change in the mean production M, $-\langle\partial_z\theta\rangle < 0$ in the upper boundary layer and coupled with the increasing vertical velocity variance at $x > 10\,\mathrm{km}$ leads to a pronounced local negative minimum in temperature flux production; in the entrainment zone $-M > B$. At $x > 19\,\mathrm{km}$, $P < 0$ but is less negative as the warm-to-warmer MABL gradually adjusts to the decaying upstream thermal overshoot. Previously, Moeng and Wyngaard (1989, Fig. 6) found that mean production M changes sign near the middle of a homogeneous convective boundary layer. Their simulations are more convectively unstable $-z_i/L \sim 18$ compared to the present calculations, but apparently similar but more complicated shear–convective dynamics are active in our MABL downstream of positive SST jumps. Again, notice temperature flux is positive in regions where $\langle\partial_z\theta\rangle > 0$, which violates the downgradient assumption used in eddy viscosity approaches (Moeng and Wyngaard 1989). Overlying the contours in Fig. 23 is the height of the zero contour $\langle w'\theta'\rangle(z) = 0$ (solid magenta line), and also the local height $\langle z_i\rangle$ (solid black line) of the maximum positive temperature gradient (Sullivan et al. 1998). Of course the quantitative values of $\langle w'\theta'\rangle$ in the entrainment zone depend on all terms in (13a), but it is encouraging that the (magenta, black) curves in Fig. 23 track the x variation of the temperature flux production.

Boundary layer entrainment is critical as it impacts scalar exchange in the lower atmosphere with the overlying troposphere and the initiation of low-level clouds (e.g., Stevens et al. 2003). Figure 24 illustrates the effect of positive SST jumps on the spatial evolution of bulk entrainment. In this figure, the normalized minimum (most negative) entrainment flux

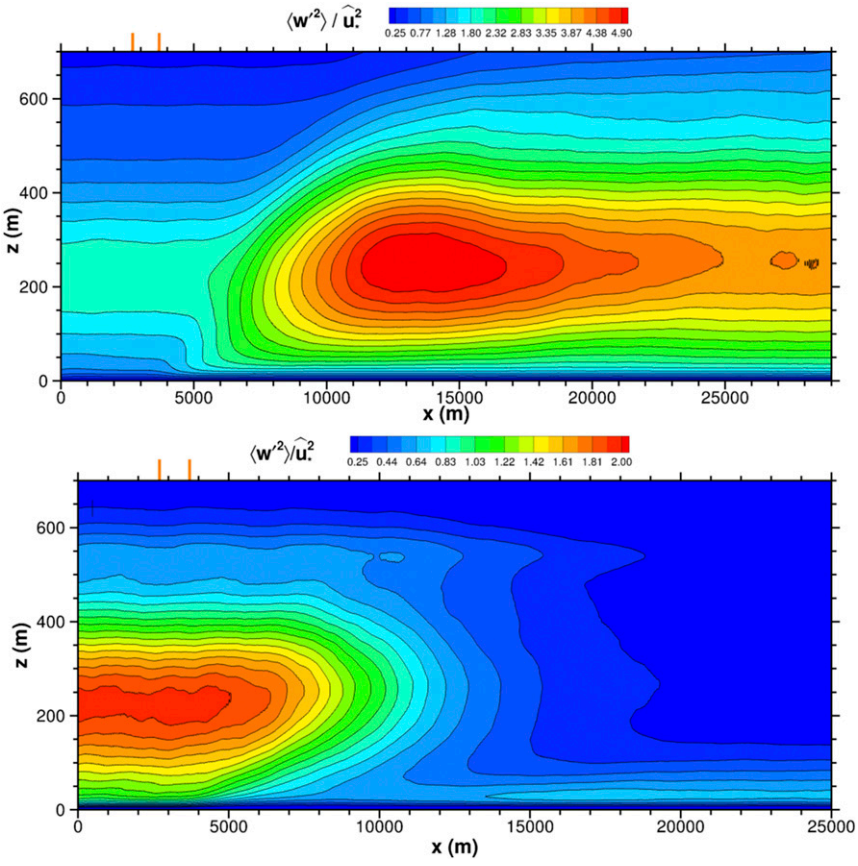

FIG. 21. Contours of vertical velocity variance for turbulent flow over (top) unstable and (bottom) stable SST fronts. The SST jump in the top and bottom panels is $\Delta\theta = 2$ K and $\Delta\theta = -1.5$ K, respectively, and $\ell = 1000$ m. The variance is normalized by $\widehat{u_*}^2$, and the orange vertical lines at the top of the panels mark the start and end location of the SST front. Note the range of the color bar is narrower in the bottom panel.

$E = \langle w'\theta' \rangle_{\min}/\widehat{Q_*}$ and the growth of the MABL $\delta z_i = \langle z_i(x) \rangle - \widehat{z_i}$ are shown on the left and right vertical axis, respectively, for $\Delta\theta > 0$, with $\ell = (1, 3, 6)$ km. Similar to other turbulence statistics, E shows a nonmonotonic variation with increasing downstream distance. In case Eu2, the maximum entrainment $-E \approx 0.6$ occurs near $x \sim 14$ km, which is well correlated with the flux production in Fig. 23. This location is more than 10 km downstream of the end of the SST jump $x_b + \ell$. For $x > 14$ km the maximum value of $-E$ retreats. For the LES considered here increases in ℓ slightly reduce the maximum value of $-E$ and shift its streamwise location downstream. The boundary layer growth δz_i is rapid and similar for the different simulations, $\langle z_i \rangle$ increases by approximately 50 m for $x = [12–29]$ km.

Notice near the right outflow boundary of domain H, $x \sim 28$ km, the entrainment flux normalized by the *local* surface temperature flux $E_\ell = E\widehat{Q_*}/\langle Q_* \rangle \sim -0.13$, that is, $-E_\ell$ is lower than the entrainment flux upstream of the SST front, see Fig. 24. This value of E_ℓ is also smaller than the entrainment flux found in other LES and DNS of homogeneous boundary layers that include both convection and shear (e.g., Moeng and Sullivan 1994; Conzemius and Fedorovich 2006; Sullivan et al. 2014; Haghshenas and Mellado 2019). The reduction in normalized entrainment flux with positive SST jumps results from a combination of effects: far downstream of the SST front the boundary layer is deeper while the interior winds in the MABL are higher because of the enhanced surface heating. The combined effects reduce the jump in wind speed Δu across the entrainment zone, thus, the impact of wind shear on entrainment flux at $x \sim 28$ km is reduced compared to its impact on entrainment flux at say $x \sim 2$ km. The DNS of Haghshenas and Mellado (2019) find shear enhances entrainment depending on the nondimensional parameter $\Delta u/N$, where N is the overlying buoyancy frequency. At the same time Δu is decreasing, the enhanced surface temperature flux far downstream of the SST jump shifts the MABL toward a more convection dominated regime with a weak overlying inversion. Under similar conditions, Deardorff et al. (1980) reports entrainment fluxes consistent with our values. The lower entrainment found at the end of domain H is further supported by the results from simulation Ehom (Fig. 22).

7. Summary and conclusions

High-Reynolds-number large-eddy simulation (LES) is used to simulate marine atmospheric boundary layers (MABL)

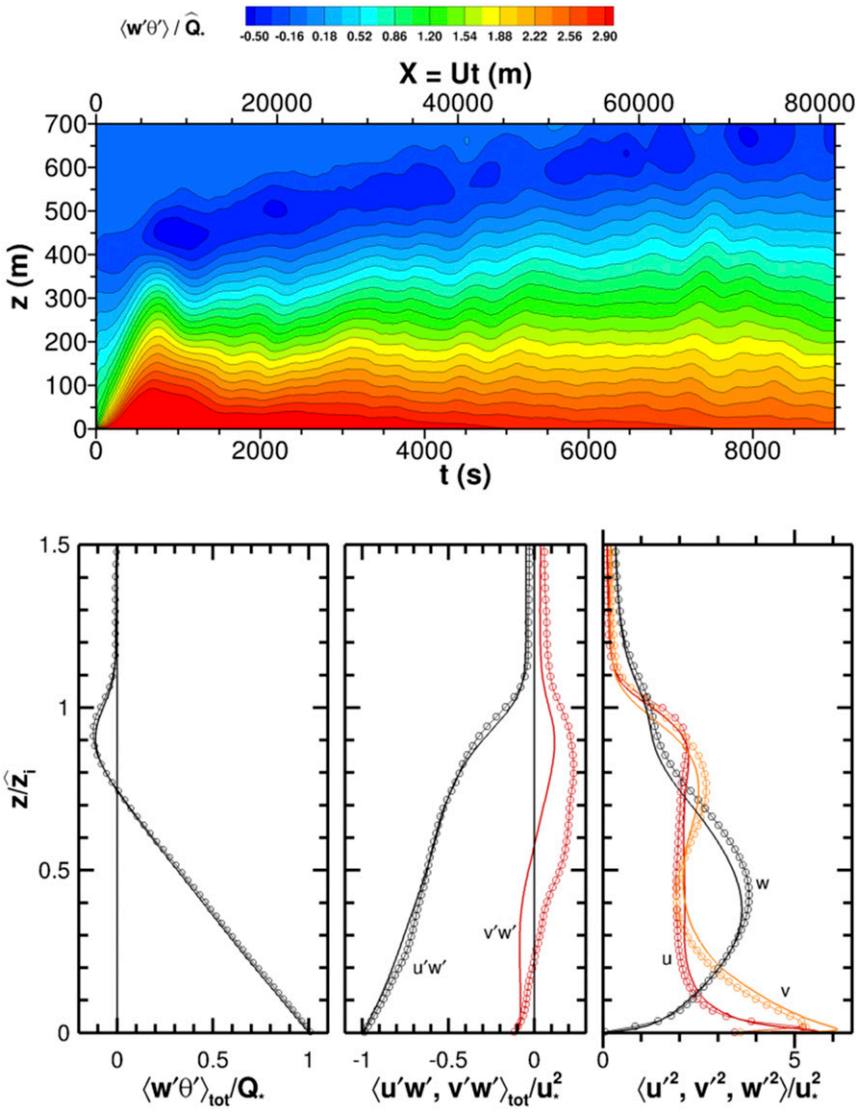

FIG. 22. Turbulence statistics from horizontally homogeneous simulation Ehom and heterogeneous simulation Eu2. (top) Contours of resolved vertical temperature flux $\langle w'\theta' \rangle$ from Ehom are shown in a t–z Hovmöller diagram. (bottom) Vertical profiles of total temperature flux, total momentum flux, and resolved variances are shown. Results from Eu2 and Ehom are shown as open circles and solid lines, respectively, and represent averages centered at $x = 27.7$ km and $t = 5000$ s. In the top panel, the average Lagrangian distance $X = Ut$, with $U = 8.6\,\mathrm{m\,s^{-1}}$.

forced by geostrophic winds $U_g = 10\,\mathrm{m\,s^{-1}}$ and spatially heterogeneous sea surface temperature (SST), that is, SST fronts. The SST heterogeneity is time invariant, varies solely in the x direction, and the imposed one-sided SST fronts feature jumps $\Delta\theta$ between two temperature levels over a finite distance ℓ. Positive and negative temperature jumps $\Delta\theta = (2, -1.5)$ K are considered with $\ell = [0.1\text{–}6]$ km. The large-scale winds are oriented perpendicular to the SST isotherms, that is, across front. Grid meshes of 2.2×10^9 points with fine resolution (horizontal, vertical) spacing $(\delta x = \delta y, \delta z) = (4.4, 2)$ m are used in a computational domain (33.75, 3.37, 1.4) km. Turbulent inflow–outflow boundary conditions are prescribed using a numerical "Fourier fringe" technique.

Turbulence passing over the SST fronts is characteristic of a weakly unstable MABL with bulk stability $-\hat{z}_i/\hat{L} = 3.7$ based on the boundary layer height $\hat{z}_i \sim 560$ m and Monin–Obukhov stability length $-\hat{L} \sim 150$ m. At this stability, the inflow turbulence features ubiquitous coherent structures, shear–convective rolls that amplify or decay in the boundary layer depending on the sign of $\Delta\theta$. The small-scale SST fronts generate perturbations that are felt over the full depth of the MABL and for extended distances downstream of the front, typically $O(20)$ km or more.

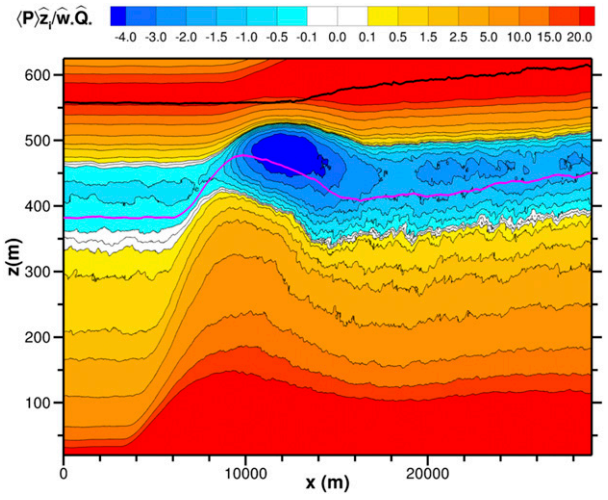

FIG. 23. Sum of production terms $P = M + B$ in the temperature flux budget, (13a), normalized by $\widehat{w_*}\widehat{Q_*}/\widehat{z_i}$ for simulation Eu2. The white contours mark the spatial location where P changes sign. The solid magenta line is the z location of the contour $\langle w'\theta'\rangle = 0$, and the solid black line is the boundary layer height $\langle z_i\rangle$ based on the maximum temperature gradient $\langle \partial_z\theta\rangle$ (Sullivan et al. 1998).

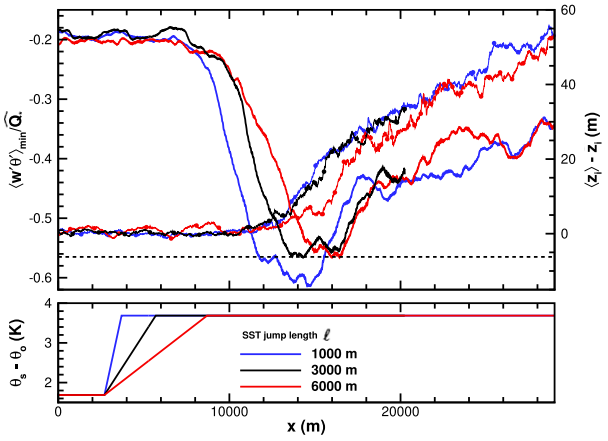

FIG. 24. (top) Variation of minimum entrainment flux $E = \langle w'\theta'\rangle_{\min}/\widehat{Q_*}$ and boundary layer height change $\delta z_i = \langle z_i\rangle - \widehat{z_i}$ downstream of positive SST gradients with $\ell = (1000, 3000, 6000)$ m; E and δz_i are indicated by lines and lines plus bullets on the left and right y axis, respectively. (bottom) The SST jump is shown. The line colors in the top panel match the line colors in the bottom panel. Upstream of the SST perturbation $E \sim -0.19$ is slightly reduced compared to a homogeneous boundary layer flow forced by constant surface temperature flux; e.g., Moeng and Sullivan (1994) and Sullivan et al. (1998). The dashed black line in the top panel marks the level $-0.19\langle Q_*\rangle/\widehat{Q_*}$, where $\langle Q_*\rangle$ is the surface temperature flux at $x \sim 28$ km, see Fig. 10.

The MABL surface layer adjusts rapidly to the SST perturbations, and in particular the local surface temperature flux Q_* closely tracks the change in SST while the response of the surface friction velocity u_* is spatially delayed especially for small ℓ and stable stratification.

The spatial transition of the MABL downstream of an SST front is nonmonotonic with increasing x featuring complex mean wind and temperature patterns and local peaks in the turbulent fluxes and vertical velocity variance. The SST fronts generate secondary wind circulations that are closed by downdrafts or updrafts near the boundary layer top. The mean temperature budget shows a primary balance between vertical divergence of turbulence temperature flux and horizontal mean advection, while the primary balance in the mean momentum budget is between horizontal advection, vertical divergence of turbulence momentum flux, and Coriolis force; horizontal pressure gradients are small. Both budgets show heterogeneous SST affects MABL dynamics including the entrainment zone. Surface $\Delta\theta > 0$ is particularly impactful as the temperature profiles develop a superadiabatic layer that extends vertically well above the traditional surface layer $0.1\widehat{z_i}$. As a result, a thermal overshoot develops approximately 10 km downstream of the SST front.

The oceanic surface is highly heterogeneous in both SST and currents over a broad range of mesoscale and submesoscale distances (McWilliams 2016). And the few LES described here are certainly not exhaustive explorations of the large parameter space spanned by the many possible combinations of winds, surface fluxes, and SST variations observed in the world's oceans, for example, Wijesekera et al. (2016) and Stevens et al. (2020, manuscript submitted to *AGU Adv.*). However, the results do provide insights and words of caution for modeling and observing heterogeneous boundary layers. The following comments are pertinent to boundary layer regimes with across-front winds and strong mean advection. Regimes with down-front winds and weak mean advection are expected to generate a different boundary layer response.

Because small-scale SST variations alter the boundary layer stability the boundary layer response varies considerably in downstream and vertical directions. Consequently, single column models need to account for nonlinear momentum and temperature flux downstream of SST heterogeneity. The approach to linear flux profiles with increasing x is nonmonotonic and depends on the sign of $\Delta\theta$. Also, single-column modeling needs to properly account for the interaction between a growing internal boundary layer (IBL) and the overlying stable inversion, that is, IBL growth is confined by the upstream boundary layer depth. Ocean submescoscale variability increases with finer resolution and our LES results suggest that boundary layer paramterizations in coupled air–sea mesoscale models need to be viewed cautiously (also see Sullivan and McWilliams 2019). Far downstream, the heterogeneous boundary layer approaches equilibrium but mean advection is nonzero, for example, in the mean temperature budget at large x vertical flux divergence is balanced by mean advection not by time tendency as in a horizontally homogeneous boundary layer. Thus, observations in the marine surface layer need spatial coverage to estimate mean advective terms. The response of boundary layer entrainment to SST heterogeneity is complex as changes in stability and interior wind speed depend on the full upstream history of boundary layer evolution, for example, enhanced entrainment is found tens of kilometers downstream from a positive jump in SST. In the case with $\Delta\theta/\ell > 0$, the vertical velocity variance reaches a maximum at an intermediate x distance that is a possible target for upward pointing lidar measurements.

The surface wind stress depends on the sign and magnitude of $\Delta\theta/\ell$, which potentially impacts the interpretation of small-scale scatterometer measurements. With $\Delta\theta > 0$, the wind stress reaches an equilibrium value a few kilometers downwind of the change in SST. The distance required to reach an equilibrium wind stress with $\Delta\theta < 0$ and $\ell < 1$ km, that is, transition to a stably stratified regime, is, however, tens of kilometers or more. Thus, divergence and curl of wind stress vary downstream of SST changes. Correlations between SST changes and changes in wind stress are likely stability dependent. The present results also show an LES "Lagrangian" approach, where a horizontally periodic domain is advected over time varying surface heterogeneity is inadequate to describe boundary layer dynamics at short time or distance from a sharp spatial change in surface conditions.

Acknowledgments. PPS and JCM were supported by the Office of Naval Research through the Physical Oceanography Program Awards N00014-17-1-2334 and N00014-18-1-2599 and by the National Oceanic and Atmospheric Administration Award NA19OAR4310378. PPS and EGP acknowledge support from the National Science Foundation and the Geophysical Turbulence Program at the National Center for Atmospheric Research. This research benefited greatly from computer resources provided by the Department of Defense High Performance Computing Modernization Program. The comments from three reviewers helped to improve the manuscript.

REFERENCES

Bishop, S. P., R. J. Small, F. O. Bryan, and R. A. Tomas, 2017: Scale dependence of midlatitude air–sea interaction. *J. Climate*, **30**, 8207–8221, https://doi.org/10.1175/JCLI-D-17-0159.1.

Chelton, D. B., and F. J. Wentz, 2005: Global microwave satellite observations of sea surface temperature for numerical weather prediction and climate research. *Bull. Amer. Meteor. Soc.*, **86**, 1097–1116, https://doi.org/10.1175/BAMS-86-8-1097.

——, M. G. Schlax, M. H. Frelich, and R. F. Miliff, 2004: Satellite measurements reveal persistent small-scale features in ocean winds. *Science*, **303**, 978–983, https://doi.org/10.1126/science.1091901.

Chen, W., M. L. Banner, E. J. Walsh, J. B. Jensen, and S. Lee, 2001: The Southern Ocean Waves Experiment. Part II: Sea surface response to wind speed and wind stress variations.*J. Phys. Oceanogr.*, **31**, 174–198, https://doi.org/10.1175/1520-0485(2001)031<0174:TSOWEP>2.0.CO;2.

Conzemius, R. J., and E. Fedorovich, 2006: Dynamics of sheared convective boundary layer entrainment. Part I: Methodological background and large-eddy simulations. *J. Atmos. Sci.*, **63**, 1151–1178, https://doi.org/10.1175/JAS3691.1.

Deardorff, J. W., 1970: A numerical study of three-dimensional turbulent channel flow at large Reynolds numbers. *J. Fluid Mech.*, **41**, 453–480, https://doi.org/10.1017/S0022112070000691.

——, G. E. Willis, and B. H. Stockton, 1980: Laboratory studies of the entrainment zone of a convectively mixed layer. *J. Fluid Mech.*, **100**, 41–64, https://doi.org/10.1017/S0022112080001000.

Durran, D. R., 1999: *Numerical Methods for Wave Equations in Geophysical Fluid Dynamics*. Springer, 476 pp.

Fairall, C. W., E. F. Bradley, J. E. Hare, A. A. Grachev, and J. B. Edson, 2003: Bulk parameterization of air–sea fluxes: Updates and verification for the COARE algorithm. *J. Climate*, **16**, 571–591, https://doi.org/10.1175/1520-0442(2003)016<0571:BPOASF>2.0.CO;2.

Fedorovich, E., F. T. M. Nieuwstadt, and R. Kaiser, 2001: Numerical and laboratory study of a horizontally evolving convective boundary layer. Part I: Transition regimes and development of the mixed layer. *J. Atmos. Sci.*, **5**, 70–86, https://doi.org/10.1175/1520-0469(2001)058<0070:NALSOA>2.0.CO;2.

——, and Coauthors, 2004: Entrainment into sheared convective boundary layers as predicted by different large eddy simulation codes. *16th Symp. on Boundary Layers and Turbulence*, Portland, ME, Amer. Meteor. Soc., P4.7, https://ams.confex.com/ams/pdfpapers/78656.pdf.

Friehe, C. A., and Coauthors, 1991: Air–sea fluxes and surface layer turbulence around a sea surface temperature front. *J. Geophys. Res.*, **96**, 8593–8609, https://doi.org/10.1029/90JC02062.

Garratt, J. R., 1992: *The Atmospheric Boundary Layer*. Cambridge University Press, 316 pp.

Garratt, J.R., 1994: Review: The atmospheric boundary layer. *Earth-Sci. Rev.*, **37**, 89–134, https://doi.org/10.1016/0012-8252(94)90026-4.

Gaube, P., C. C. Chickadel, R. Branch, and A. Jessup, 2019: Satellite observations of SST-Induced wind speed perturbation at the oceanic submesoscale. *Geophys. Res. Lett.*, **46**, 2690–2695, https://doi.org/10.1029/2018GL080807.

Gemmrich, J., and A. Monahan, 2018: Covariability of near-surface wind speed statistics and mesoscale sea surface temperature fluctuations. *J. Phys. Oceanogr.*, **48**, 465–478, https://doi.org/10.1175/JPO-D-17-0177.1.

Gill, A. E., 1982: *Atmosphere–Ocean Dynamics*. Academic Press, 662 pp.

Gropp, W., S. Huss-Lederman, A. Lumsdaine, E. Lusk, B. Nitzberg, W. Saphir, and M. Snir, 1998: *The MPI-2 Extensions*. Vol. 2, *MPI: The Complete Reference*, MIT Press, 344 pp.

Gula, J., M. J. Molemaker, and J. C. McWilliams, 2014: Submesoscale cold filaments in the Gulf Stream. *J. Phys. Oceanogr.*, **44**, 2617–2643, https://doi.org/10.1175/JPO-D-14-0029.1.

Haghshenas, A., and J. P. Mellado, 2019: Characterization of wind-shear effects on entrainment in a convective boundary layer. *J. Fluid Mech.*, **858**, 145–183, https://doi.org/10.1017/jfm.2018.761.

Inoue, M., G. Matheou, and J. Teixeira, 2014: LES of a spatially developing atmospheric boundary layer: Application of a fringe method for the stratocumulus to shallow cumulus cloud transition. *Mon. Wea. Rev.*, **142**, 3418–3424, https://doi.org/10.1175/MWR-D-13-00400.1.

Jiang, Q., Q. Wang, S. Wang, and S. Gaberšek, 2020: Turbulence adjustment and scaling in an offshore convective internal boundary layer: A CASPER case study. *J. Atmos. Sci.*, **77**, 1661–1681, https://doi.org/10.1175/JAS-D-19-0189.1.

Kaimal, J. C., and J. J. Finnigan, 1994: *Atmospheric Boundary Layer Flows*. Oxford University Press, 289 pp.

Khalsa, S. J. S., and G. K. Greenhut, 1989: Atmospheric turbulence structure in the vicinity of an oceanic front. *J. Geophys. Res.*, **94**, 4913–4922, https://doi.org/10.1029/JC094iC04p04913.

Kilpatrick, T., N. Schneider, and B. Qiu, 2014: Boundary layer convergence induced by strong winds across a midlatitude SST front. *J. Climate*, **27**, 1698–1718, https://doi.org/10.1175/JCLI-D-13-00101.1.

Large, W. G., and S. Pond, 1981: Open ocean flux measurements in moderate to strong winds. *J. Phys. Oceanogr.*, **11**, 324–336, https://doi.org/10.1175/1520-0485(1981)011<0324:OOMFMI>2.0.CO;2.

Lin, C.-L., C.-H. Moeng, P. P. Sullivan, and J. McWilliams, 1997: The effect of surface roughness on flow structures in a neutrally stratified planetary boundary layer flow. *Phys. Fluids*, **9**, 3235–3249, https://doi.org/10.1063/1.869439.

Lüpkes, C., V. M. Gryanik, B. Witha, M. Gryschka, S. Raasch, and T. Gollnik, 2008: Modelling convection over Arctic leads with LES and a non-eddy-resolving microscale model. *J. Geophys. Res.*, **113**, C09028, https://doi.org/10.1029/2007JC004099.

Mayor, S. D., P. R. Spalart, and G. J. Tripoli, 2002: Application of a perturbation recycling method in the large-eddy simulation of a mesoscale convective internal boundary layer. *J. Atmos. Sci.*, **59**, 2385–2395, https://doi.org/10.1175/1520-0469(2002)059<2385:AOAPRM>2.0.CO;2.

McWilliams, J. C., 2016: Submesoscale currents in the ocean. *Proc. Roy. Soc. London*, **A472**, 20160117, https://doi.org/10.1098/RSPA.2016.0117.

——, C.-H. Moeng, and P. P. Sullivan, 1999: Turbulent fluxes and coherent structures in marine boundary layers: Investigations by large-eddy simulation. *Air–Sea Exchange: Physics, Chemistry, Dynamics, and Statistics*, G. Geernaert, Ed., Kluwer, 507–538.

Meroni, A. N., M. Giurato, F. Ragone, and C. Pasquero, 2020: Observational evidence of the preferential occurrence of wind convergence over sea surface temperature fronts in the Mediterranean. *Quart. J. Roy. Meteor. Soc.*, **728**, 1443–1458, https://doi.org/10.1002/QJ.3745.

Mironov, D. V., and P. P. Sullivan, 2016: Second-moment budgets and mixing intensity in the stably stratified atmospheric boundary layer over thermally heterogeneous surfaces. *J. Atmos. Sci.*, **73**, 449–464, https://doi.org/10.1175/JAS-D-15-0075.1.

Moeng, C.-H., 1984: A large-eddy simulation model for the study of planetary boundary-layer turbulence. *J. Atmos. Sci.*, **41**, 2052–2062, https://doi.org/10.1175/1520-0469(1984)041<2052:ALESMF>2.0.CO;2.

——, and J. C. Wyngaard, 1989: Evaluation of turbulent transport and dissipation closures in second-order modeling. *J. Atmos. Sci.*, **46**, 2311–2330, https://doi.org/10.1175/1520-0469(1989)046<2311:EOTTAD>2.0.CO;2.

——, and P. P. Sullivan, 1994: A comparison of shear- and buoyancy-driven planetary boundary layer flows. *J. Atmos. Sci.*, **51**, 999–1022, https://doi.org/10.1175/1520-0469(1994)051<0999:ACOSAB>2.0.CO;2.

——, and ——, 2015: Large-eddy simulation. *Encyclopedia of Atmospheric Sciences*, 2nd ed. G. R. North, F. Zhang, and J. Pyle, Eds., Vol. 4, Academic Press, 232–240.

Munters, W., C. Meneveau, and J. Meyers, 2016: Turbulent inflow precursor method with time-varying direction for large-eddy simulations and applications to wind farms. *Bound.-Layer Meteor.*, **159**, 305–328, https://doi.org/10.1007/s10546-016-0127-z.

Muñoz-Esparza, D., B. Kosović, J. van Beeck, and J. Mirocha, 2015: A stochastic perturbation method to generate inflow turbulence in large-eddy simulation models: Application to neutrally stratified atmospheric boundary layers. *Phys. Fluids*, **27**, 035102, https://doi.org/10.1063/1.4913572.

Nordström, J., N. Nordin, and D. Henningson, 1999: The fringe region technique and the Fourier method used in the direct numerical simulation of spatially evolving viscous flows. *SIAM J. Sci. Comput.*, **20**, 1365–1393, https://doi.org/10.1137/S1064827596310251.

O'Neill, L. W., D. B. Chelton, and S. K. Esbensen, 2010: The effects of SST-induced surface wind speed and direction gradients on midlatitude surface vorticity and divergence. *J. Climate*, **23**, 255–281, https://doi.org/10.1175/2009JCLI2613.1.

Perlin, N., S. P. de Szoke, D. B. Chelton, R. M. Samelson, E. D. Skyllingstad, and L. W. O'Neill, 2014: Modeling the atmospheric boundary layer wind response to mesoscale sea surface temperature perurbations. *Mon. Wea. Rev.*, **142**, 4284–4307, https://doi.org/10.1175/MWR-D-13-00332.1.

Plagge, A., J. B. Edson, and D. Vandemark, 2016: In situ and satellite evaluation of air–sea flux variation near ocean temperature gradients. *J. Climate*, **29**, 1583–1602, https://doi.org/10.1175/JCLI-D-15-0489.1.

Redelsperger, J.-L., M.-N. Bouin, J. Pianezze, V. Garnier, and L. Marié, 2019: Impact of a sharp, small-scale SST front on the marine atmospheric boundary layer on the Iroise Sea: Analysis from a hectometric simulation. *Quart. J. Roy. Meteor. Soc.*, **145**, 3692–3714, https://doi.org/10.1002/qj.3650.

Renault, L., P. Marchesiello, S. Masson, and J. C. McWilliams, 2019: Remarkable control of western boundary currents by *eddy killing*, a mechanical air–sea coupling process. *Geophys. Res. Lett.*, **46**, 2743–2751, https://doi.org/10.1029/2018GL081211.

Samelson, R. M., E. D. Skyllingstad, D. B. Chelton, S. K. Esbensen, L. W. O'Neill, and N. Thum, 2006: On the coupling of wind stress and sea surface temperature. *J. Climate*, **19**, 1557–1566, https://doi.org/10.1175/JCLI3682.1.

Schlatter, P., N. A. Adams, and L. Kleiser, 2005: A windowing method for periodic inflow/outflow boundary treatment of non-periodic flows. *J. Comput. Phys.*, **206**, 505–535, https://doi.org/10.1016/j.jcp.2004.12.015.

Schmidt, H., and U. Schumann, 1989: Coherent structure of the convective boundary layer derived from large-eddy simulations. *J. Fluid Mech.*, **200**, 511–562, https://doi.org/10.1017/S0022112089000753.

Seo, H., A. J. Miller, and J. R. Norris, 2016: Eddy-wind interaction in the California current system: Dynamics and impacts. *J. Phys. Oceanogr.*, **46**, 439–459, https://doi.org/10.1175/JPO-D-15-0086.1.

Shao, M., and Coauthors, 2019: The variability of winds and fluxes observed near submeoscale fronts. *J. Geophys. Res. Oceans*, **124**, 7756–7780, https://doi.org/10.1029/2019JC015236.

Skyllingstad, E. D., R. M. Samelson, L. Mahrt, and P. Barbour, 2005: A numerical modeling study of warm off-shore flow over cool water. *Mon. Wea. Rev.*, **133**, 345–361, https://doi.org/10.1175/MWR-2845.1.

——, D. Vickers, L. Mahrt, and R. Samelson, 2007: Effects of mesoscale sea-surface temperature fronts on the marine atmospheric boundary layer. *Bound.-Layer Meteor.*, **123**, 219–237, https://doi.org/10.1007/s10546-006-9127-8.

——, S. P. de Szoeke, and L. W. O'Neill, 2019: Modeling the transient response of tropical convection to mesoscale SST variations. *J. Atmos. Sci.*, **76**, 1227–1244, https://doi.org/10.1175/JAS-D-18-0079.1.

Small, R. J., and Coauthors, 2008: Air–sea interaction over ocean fronts and eddies. *Dyn. Atmos. Oceans*, **45**, 274–319, https://doi.org/10.1016/j.dynatmoce.2008.01.001.

Spalart, P. R., and J. H. Watmuff, 1993: Experimental and numerical study of a turbulent boundary layer with pressure gradients. *J. Fluid Mech.*, **249**, 337–371, https://doi.org/10.1017/S002211209300120X.

Spall, M. A., 2007: Midlatitude wind stress–sea surface temperature coupling in the vicinity of oceanic fronts. *J. Climate*, **20**, 3785–3801, https://doi.org/10.1175/JCLI4234.1.

Stevens, B., and Coauthors, 2003: Dynamics and chemistry of marine stratocumulus—DYCOMS-II. *Bull. Amer. Meteor. Soc.*, **84**, 579–594, https://doi.org/10.1175/BAMS-84-5-579.

Stull, R. B., 1988: *An Introduction to Boundary Layer Meteorology*. Kluwer Academic Publishers, 666 pp.

Sullivan, P. P., and J. C. McWilliams, 2010: Dynamics of winds and currents coupled to surface waves. *Annu. Rev. Fluid. Mech.*, **42**, 19–42, https://doi.org/10.1146/annurev-fluid-121108-145541.

——, and E. G. Patton, 2011: The effect of mesh resolution on convective boundary-layer statistics and structures generated by large-eddy simulation. *J. Atmos. Sci.*, **68**, 2395–2415, https://doi.org/10.1175/JAS-D-10-05010.1.

——, and J. C. McWilliams, 2019: Langmuir turbulence and filament frontogenesis in the oceanic surface boundary layer. *J. Fluid Mech.*, **879**, 512–553, https://doi.org/10.1017/jfm.2019.655.

——, ——, and C.-H. Moeng, 1994: A subgrid-scale model for large-eddy simulation of planetary boundary-layer flows. *Bound.-Layer Meteor.*, **71**, 247–276, https://doi.org/10.1007/BF00713741.

——, ——, and ——, 1996: A grid nesting method for large-eddy simulation of planetary boundary layer flows. *Bound.-Layer Meteor.*, **80**, 167–202, https://doi.org/10.1007/BF00119016.

——, C.-H. Moeng, B. Stevens, D. H. Lenschow, and S. D. Mayor, 1998: Structure of the entrainment zone capping the convective atmospheric boundary layer. *J. Atmos. Sci.*, **55**, 3042–3064, https://doi.org/10.1175/1520-0469(1998)055<3042:SOTEZC>2.0.CO;2.

——, J. C. McWilliams, and E. G. Patton, 2014: Large-eddy simulation of marine boundary layers above a spectrum of moving waves. *J. Atmos. Sci.*, **71**, 4001–4027, https://doi.org/10.1175/JAS-D-14-0095.1.

——, J. C. Weil, E. G. Patton, H. J. J. Jonker, and D. V. Mironov, 2016: Turbulent winds and temperature fronts in large-eddy simulations of the stable atmospheric boundary layer. *J. Atmos. Sci.*, **73**, 1815–1840, https://doi.org/10.1175/JAS-D-15-0339.1.

Tetzlaff, A., C. Lüpkes, and J. Hartmann, 2015: Aircraft-based observations of atmospheric boundary-layer modification over Arctic leads. *Quart. J. Roy. Meteor. Soc.*, **141**, 2839–2856, https://doi.org/10.1002/qj.2568.

Wenegrat, J. O., and R. S. Arthur, 2018: Response of the atmospheric boundary layer to submesoscale sea-surface temperature fronts. *Geophys. Res. Lett.*, **45**, 13 505–13 512, https://doi.org/10.1029/2018GL081034.

Wijesekera, H. W., and Coauthors, 2016: ASIRI: An ocean–atmosphere initiative for Bay of Bengal. *Bull. Amer. Meteor. Soc.*, **97**, 1859–1884, https://doi.org/10.1175/BAMS-D-14-00197.1.

Wyngaard, J. C., 2010: *Turbulence in the Atmosphere*. Cambridge University Press, 393 pp.